nature genetics

Article

https://doi.org/10.1038/s41588-025-02407-8

Spatially resolved multi-omics of human metabolic dysfunction-associated steatotic liver disease

Received: 27 July 2024

Accepted: 13 October 2025

Published online: 24 November 2025

Check for updates

Ziyu Li[1,17], Gang Luo[2,3,4,5,6,17], Changpei Gan[2,3,4,5,17], Huayu Zhang[2,3,4,5,17], Ling Li[2,3,4,5,17], Xiaoxun Zhang[2,3,4,5], Xudong Xing[7], Simeng Hu[8], Xu Tan[9], Jingjing Ding[2,3,4,5], Liangjun Zhang[2,3,4,5], Ying Peng[2,3,4,5], Ziqian Xu[2,3,4,5], Qiong Pan[2,3,4,5], Christopher D. Byrne[10], Giovanni Targher[11], Xiao-Zhi Jin[12], Wei Xie[12], Xinshou Ouyang[13] ✉, Ming-Hua Zheng[12,14] ✉, Fan Bai[1,15,16] ✉ & Jin Chai[2,3,4,5] ✉

Metabolic dysfunction-associated steatotic liver disease (MASLD) is a leading cause of chronic liver disease worldwide. We generated single-cell and spatial transcriptomic and metabolomic maps from 61 human livers, including controls ($n = 10$), metabolic dysfunction-associated steatotic liver (MASL) ($n = 17$) and metabolic dysfunction-associated steatohepatitis (MASH) ($n = 34$). We identified microphthalmia-associated transcription factor (MITF) as a key regulator of the lipid-handling capacity of lipid-associated macrophages (LAMs), and further revealed a hepato-protective role of LAMs mediated through hepatocyte growth factor secretion. Unbiased deconvolution of spatial transcriptomics delineated a fibrosis-associated gene program enriched in advanced MASH, suggesting profibrotic crosstalk between central vein endothelial and hepatic stellate cells within fibrotic regions. Mass spectrometry imaging-based spatial metabolomics demonstrated MASLD-specific accumulation of phospholipids, potentially linked to lipoprotein-associated phospholipase A_2-mediated phospholipid metabolism in LAMs. This spatially resolved multi-omics atlas of human MASLD, which can be queried at the Human Masld Spatial Multiomics Atlas, provides a valuable resource for mechanistic and therapeutic studies.

Metabolic dysfunction-associated steatotic liver disease (MASLD) is a progressive disease that starts with isolated steatosis (metabolic dysfunction-associated steatotic liver (MASL)) and can evolve to a more severe stage known as metabolic dysfunction-associated steatohepatitis (MASH), during which chronic liver injury, inflammation and varying degrees of fibrosis are superimposed on the initial steatosis. MASH has the potential to advance further toward cirrhosis and hepatocellular carcinoma[1,2].

High-resolution approaches, such as single-cell RNA sequencing (scRNA-seq) and single-nucleus RNA sequencing (snRNA-seq) have provided paradigm shifts in our understanding of the cellular and molecular mechanisms underlying MASLD pathogenesis[3–6], complementing fundamental elements for the canonical conceptual framework known as the substrate overload liver injury model[7], where hepatocyte lipotoxicity is regarded as the initiating factor, triggering a cascade of events mediated by diverse non-parenchymal cell (NPC)

A full list of affiliations appears at the end of the paper. ✉e-mail: xinshou.ouyang@yale.edu; zhengmh@wmu.edu.cn; fbai@pku.edu.cn; jin.chai@cldcsw.org

subpopulations, such as liver endothelial cells (LECs), tissue-resident Kupffer cells (KCs), hepatic stellate cells (HSCs), cholangiocytes and several immune cell types that synergistically escalate hepatic steatosis, inflammation and fibrosis. For example, HSCs are activated by osteopontin (OPN), encoded by *SPP1*, and Hedgehog ligands secreted by reprogrammed hepatocytes[8]. Activated HSCs function as a central hub of intrahepatic signaling, releasing stellakines, which have a profibrotic role during MASLD progression and may ultimately result in end-stage liver disease[3].

Accumulating evidence highlights the pivotal role of lipid-associated macrophages (LAMs), which are marked by increased expression of triggering receptor on myeloid cells 2 (TREM2), in maintaining the immune and metabolic homeostasis within the fatty liver[3,9–11]. Despite the importance of LAMs in human MASLD pathogenesis, the mechanisms through which LAMs develop a lipid-handling and immune-suppressive phenotype remain poorly understood. A deeper understanding of how blood-derived monocytes differentiate into LAMs could provide therapeutic insights, particularly in modulating their involvement in the onset and resolution phases of chronic liver diseases.

Although single-cell analysis has provided valuable insights into the heterogeneity of liver NPCs and their dynamic changes throughout MASLD progression, it is limited by the lack of spatial organization information. Hepatocytes operate in well-organized repeating anatomical units known as liver lobules. Key liver functions are expressed nonuniformly across the lobule axis because of gradients of oxygen, nutrients and hormones, a phenomenon known as zonation[12,13]. The division of metabolic tasks and the spatially polarized immune system reinforces the necessity to interrogate the pathogenesis of MASLD in a spatially resolved context, an area that is relatively underexplored.

Spatial transcriptomics (ST) enables the profiling of the spatial distribution of RNA and cell–cell interactions (CCIs) within individual tissue sections[14]. The introduction of ST into liver tissue transcriptome-wide profiling has substantially advanced the understanding of the mechanisms regulating liver regeneration[15] and the niche signals involved in region-specific cholangiopathies[16], while its application to human MASLD remains unexplored. A comprehensive MASLD atlas would also require metabolomic profiling to better elucidate the region-specific metabolic alterations and cell-type-specific metabolic functions. Mass spectrometry imaging (MSI)-based spatial metabolomics (SM) provides a label-free, spatially resolved measurement of metabolite abundance directly from fresh-frozen tissue sections[17,18]. Because of experimental constraints, it is currently applied as separate methodologies alongside ST[19]. The lack of an in silico spatial multimodal analysis (SMA) pipeline integrating SM and ST data limits our ability to interpret the complex interplay between metabolic dysfunction and hepatic inflammation.

In this study, we used a combination of single-cell gene expression, unbiased ST, SM and spatial proteomics (SP) approaches to decode MASLD-relevant gene and metabolite expression programs within their spatial contexts. Adjacent frozen liver biopsy sections from patients with MASL and MASH, and resection samples from controls, were prepared to perform ST and SM, providing a spatially resolved atlas of metabolite and gene expression patterns throughout disease progression. SMA of ST and SM modalities was achieved by aligning the MSI data points directly to the hematoxylin and eosin (H&E)-stained image used for ST, enabling the simultaneous measurements of mRNA transcripts and metabolites within the same tissue microregions. In total, we obtained high-quality transcriptomes of 540,216 single cells and 47,864 Visium ST spots and metabolomes from 841,534 MSI data points. The processed spatially resolved multi-omics datasets are fully accessible on the browsable web portal of the Human Masld Spatial Multiomics Atlas, providing a resource for data download and spatial visualization of gene and metabolite expression.

Results

Single-cell and spatial transcriptional profiling of MASLD human livers

We applied scRNA-seq, scVDJ-seq, ST (10x Visium) and SM (matrix-assisted laser desorption ionization (MALDI)–MSI) to resected or biopsy liver samples collected from 61 individuals across the different stages of MASLD progression defined by histology as control (CTRL, $n = 10$), MASL ($n = 17$) and MASH ($n = 34$) (Fig. 1a,b and Supplementary Table 1). MSI-based SM was performed on a subset of tissue sections ($n = 27$) adjacent to those used for Visium ST ($n = 35$) (Supplementary Notes), enabling integrative SMA.

After meticulous quality control and computational doublet calling (Extended Data Fig. 1a and Supplementary Table 2), we obtained single-cell transcriptomes for 540,216 cells across 58 libraries generated from 29 samples ($n = 6$ CTRL, $n = 7$ MASL, and $n = 16$ MASH) for downstream analysis (Fig. 1b,c). Each sample was profiled using two libraries, one for parenchymal cells and another for NPCs (Supplementary Notes). We identified 17 cell types that were manually annotated based on the RNA expression of known markers (Extended Data Fig. 1b), categorized into four broad cell-type groups as follows: hepatic $CD45^-$ cells, T lymphoid (T) and natural killer (NK) cells, B lymphocytes and myeloid cells. Neutrophils and mast cells were excluded from the myeloid compartment for subsequent cellular abundance analysis because of their low cell capture efficiency during tissue dissociation and high susceptibility to RNA degradation caused by elevated RNase activity, which collectively introduces higher technical noise and limits their accurate measurement. Within the hepatic $CD45^-$ cell compartment (82,011 cells), LECs exhibited marked zonation-related transcriptomic heterogeneity and were subclustered into three subsets based on the expression of canonical gene markers as follows: liver sinusoidal endothelial cells (LSECs), marked by *STAB2* and *CLEC1B*, central vein ECs (marked by *RSPO3* and *WNT2*) and portal vein ECs (marked by *SLCO2A1*, *MECOM*, *PODXL* and *JAG1*)[16].

To contextualize the cell types and states identified using scRNA-seq within tissue micro-environments, we performed ST analysis using 10x Visium ($n = 7$ CTRL, $n = 10$ MASL and $n = 18$ MASH), adding a key dimension to the field of MASLD. A total of 47,864 spots were ordered along a spatial trajectory annotated as portal, periportal, mid and central based on known lobule zonation markers[20] (Fig. 1d–f and Extended Data Fig. 1c).

MASLD remodels immune cell composition and repertoires within the liver microenvironment

Within the T and NK compartment (258,618 cells), we used canonical lineage markers to identify seven major cell types: mucosal-associated invariant T (MAIT) cells, regulatory T (T_{reg}) cells, $CD8^+$ effector T (T_{eff}) cells, CD4/CD8 naive T cells, circulating natural killer T (NKT) cells, resident NK cells and circulating NK cells (Fig. 2a and Extended Data Fig. 2a). To reveal the compositional changes between MASLD and CTRLs in this compartment, we performed Milo differential abundance testing[21] (Fig. 2b). We found a prominent increase in all five T cell clusters and a decrease in resident NK cells in patients with MASLD compared to CTRLs, yet no cluster exhibited a significant difference in abundance between MASH and MASL (Fig. 2c–e). To investigate the clonal relationship among individual T cells across three disease conditions[22], we performed T cell receptor (TCR) analysis for five T and NK cell subsets except for resident and circulating NK cells. We examined whether expanded clonotypes were shared among each sample, across disease conditions and among cell types. Large clonal expansions were observed particularly in CD8 T_{eff} cells and MAITs from patients with MASLD (Fig. 2f). While most expanded clonotypes in CD8 T_{eff} cells were unique to individual patients, the large expanded clonotypes in MAITs were shared among individuals. Notably, circulating NKT cells exhibited clonal expansion predominantly under diseased conditions

https://doi.org/10.1038/s41588-025-02407-8

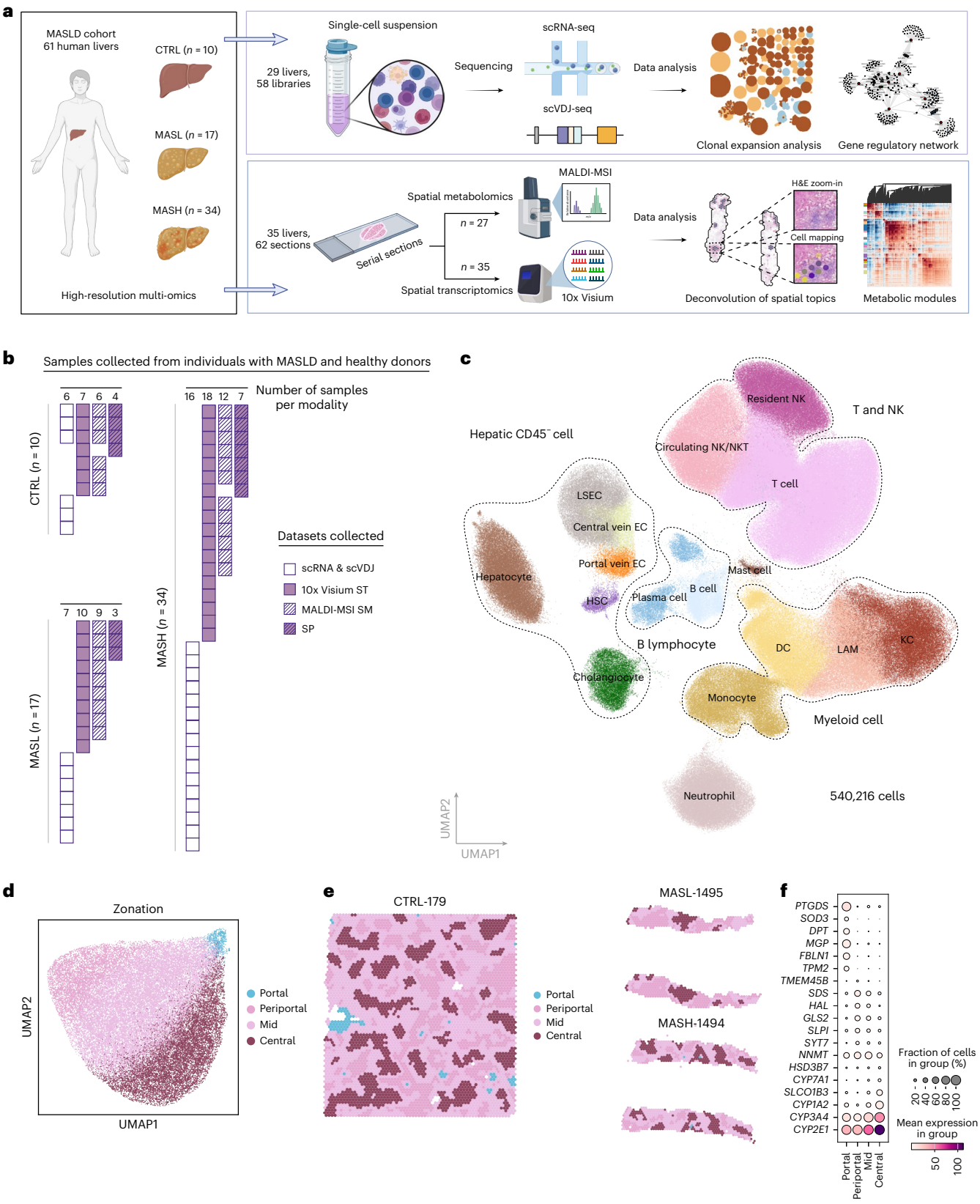

Fig. 1 | Spatial and single-cell transcriptomic atlas of human MASLD. a, Scheme of the multi-omics spatial human MASLD atlas experimental and analysis workflow. **b**, Summary of the samples in this study, with each row representing an individual and the columns indicating the modalities assayed. **c**, Uniform manifold approximation and projection (UMAP) plot of 540,216 cells profiled using scRNA-seq and colored according to cell type in CTRL ($n = 6$), MASL ($n = 7$) and MASH ($n = 16$). **d**, UMAP visualizations where the dots correspond to individual spots for 48,154 spots profiled with 10x Visium, colored according to liver lobular zones. **e**, Spatial distribution of four liver lobular zones (portal, periportal, mid and central) in three tissue sections taken from the CTRL, MASL and MASH groups, respectively. **f**, Dot plot showing the expression of lobule zone marker genes across four liver lobular zones. **a**, The illustration was created with BioRender.com.

https://doi.org/10.1038/s41588-025-02407-8

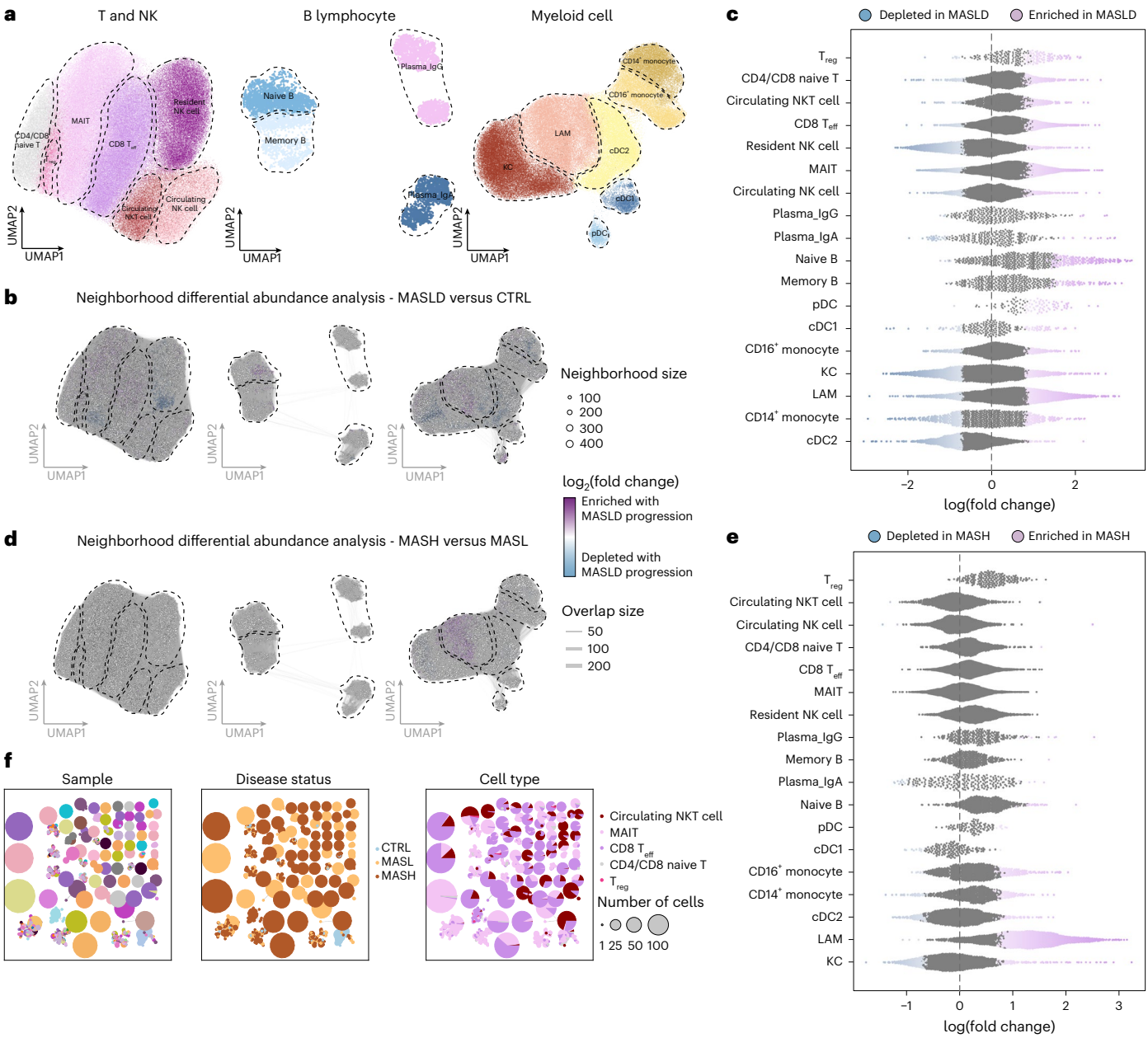

Fig. 2 | MASLD progression affects the homeostatic cellular state of the liver microenvironment. a, UMAP plots of T and NK cells, B lymphocytes and myeloid cells, colored according to cell type. **b**, Graphical representation of the Nhoods identified using Milo. Nodes are Nhoods, colored according to their $\log_2$(fold change) between MASL/MASH ($n = 23$) and CTRL ($n = 6$), blocking for the effects of the scRNA-seq library (parenchymal or non-parenchymal). Nondifferential abundance Nhoods (FDR ≥ 0.05) are colored white. **c**, Beeswarm plot of the $\log_2$(fold change) in the Milo neighborhoods between MASL/MASH and CTRL, grouped into each cell type. Nhoods with significant change in cellular abundance are colored as in **b**. **d**, Graph representation of Nhoods identified using Milo. Nodes are Nhoods, colored according to their $\log_2$(fold change) between MASH ($n = 16$) and MASL ($n = 7$), blocking for the effects of the scRNA-seq library. Nondifferential abundance Nhoods (FDR ≥ 0.05) are colored white. **e**, Beeswarm plot of the $\log_2$(fold change) in the Milo neighborhoods between MASH and MASL, grouped into each cell type. Nhoods with significant change in cellular abundance are colored as in **d**. **f**, Network plots showing the similarity of the TCRα and TCRβ CDR3 amino acid sequences for each sample, disease status and cell type. Clonotype clusters with clonal size ≥ 20 are selected.

(Fig. 2f), suggesting that the clonal expansion of circulating NKT cells may contribute to the progression of MASLD.

We subclustered 17,576 cells, manually annotated as B and plasma cells, obtaining four subsets based on their expression of canonical markers: naive B cells, memory B cells, IgG plasma (plasma_IgG) cells and IgA plasma (plasma_IgA) cells (Fig. 2a and Extended Data Fig. 2b). The proportions of naive B and memory B cells increased in patients with MASLD compared to CTRLs. Like the T and NK compartment results, no cluster of B cells showed a significant difference in abundance between MASH and MASL (Fig. 2b–e). However, B cell receptor (BCR) analysis revealed a trend toward a larger clonal expansion of plasma_IgA and plasma_IgG cells in MASH compared to the MASL group, with minimal clonotypes sharing between patients with MASLD and CTRLs or among individual patients (Extended Data Fig. 2d,e).

To characterize the transcriptome dynamics in 130,671 cells of the myeloid compartment across disease conditions, we further subclustered monocytes into two subsets and dendritic cells (DCs) into three subsets based on the expression of canonical gene markers as follows: CD14$^+$ monocytes, CD16$^+$ monocytes, plasmacytoid DCs (pDCs), conventional type 1 DCs (cDC1s), conventional type 2 DCs (cDC2s)

https://doi.org/10.1038/s41588-025-02407-8

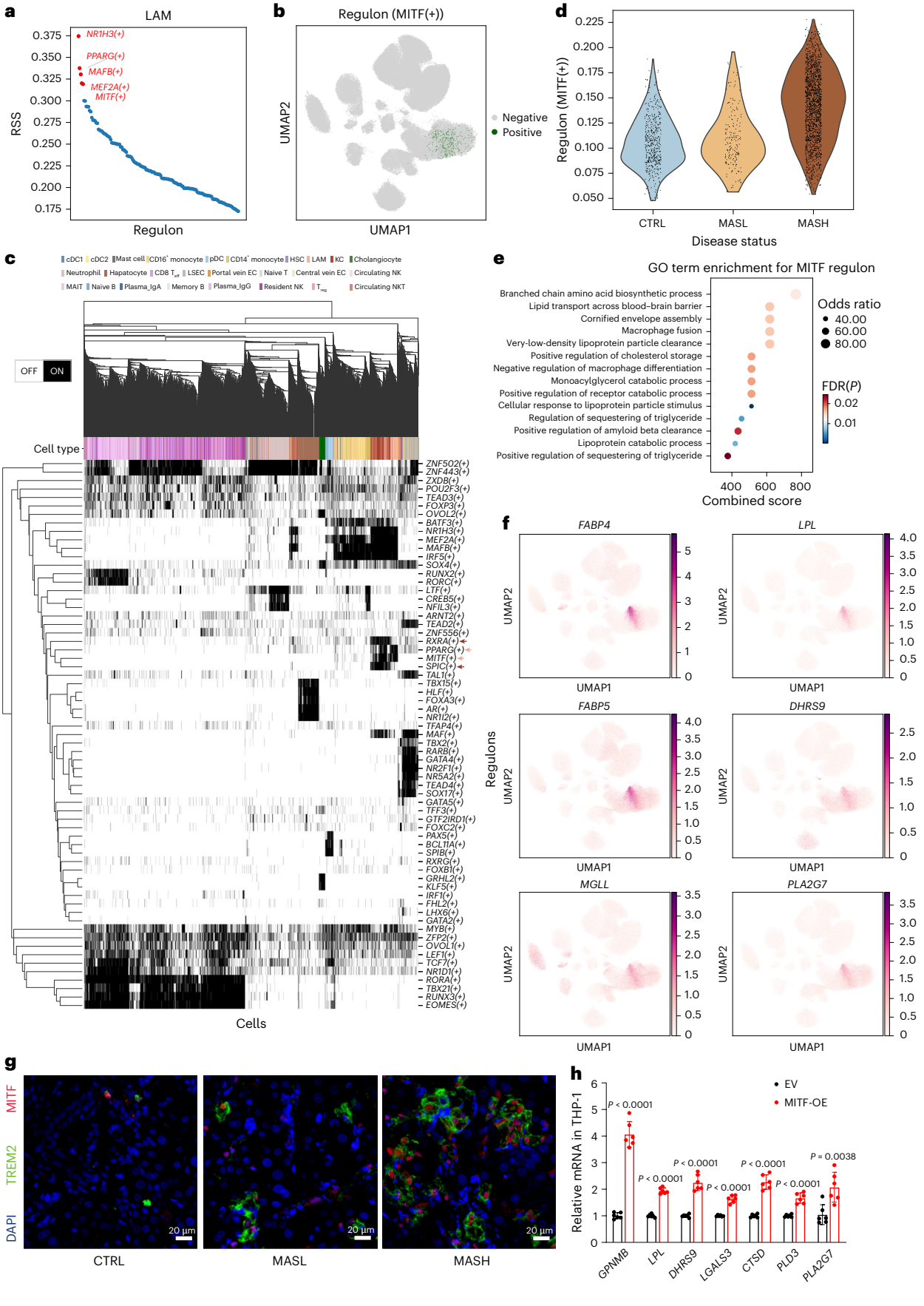

Fig. 3 | Identification of MITF as a LAM-specific TF. a, Regulon specificity score (RSS) for LAMs; the top five regulons are highlighted in red and labeled on the plot, while the specificity score is shown on the *y* axis. **b**, Binarized activity of the MITF regulon for each cell generated from the SCENIC area under the curve (AUC) distribution, displayed in the UMAP space with green spots representing cells that are activated. **c**, Binarized activity of selected regulons, representing the union of the top five regulons most specific to each cell type, plotted as a heatmap with the black blocks indicating cells that are 'on'. The peach and russet arrows indicate LAM-specific and KC-specific TFs, respectively. **d**, Violin plot showing the MITF regulon activity score in LAMs from the CTRL, MASL and MASH groups. **e**, Top GO terms enriched by overrepresentation analysis (ORA) for the top 100 target genes of the MITF regulon. *P* values were computed using a two-sided Fisher's exact test and adjusted for multiple testing using the Benjamini–Hochberg procedure. **f**, Expression of six MITF-targeted lipid-metabolism-related genes in the scRNA-seq dataset displayed in the UMAP space. **g**, Representative IF protein staining of MITF and TREM2 for tissue specimens from the CTRL, MASL and MASH groups ($n = 3$ independent experiments). **h**, Expression of *GPNMB*, *LPL*, *DHRS9*, *LGALS3*, *CTSD*, *PLD3* and *PLA2G7* using quantitative PCR with reverse transcription (RT–qPCR) in THP-1 cells after *MITF*-OE compared to empty vector (EV) ($n = 6$ biological replicates). Data are presented as mean values ± s.d.; statistical significance was determined using an unpaired, two-sided Student's *t*-test. DAPI, 4′,6-diamidino-2-phenylindole.

(Fig. 2a and Extended Data Fig. 2c). The proportions of pDCs and LAMs increased, whereas the proportion of cDC2s declined predominantly in patients with MASLD compared to CTRLs (Fig. 2b,c). Differential abundance analysis based on disease severity revealed a decrease in KCs and an increase in $CD14^+$ and $CD16^+$ monocytes, alongside a marked expansion of LAMs in MASH compared to MASL (Fig. 2d,e).

Together, these findings delineated how MASLD progression reshapes the immune cell composition and repertoires within the liver microenvironment. The clonal expansion of circulating NKT cells emerged as a distinct feature among patients with MASLD. While most immune cell types showed no significant differences in abundance between MASH and MASL, LAMs exhibited a pronounced increase with disease severity, particularly within the pericentral area (Extended Data Fig. 2f), underscoring their potential role in MASLD progression.

Microphthalmia-associated transcription factor shapes the lipid-handling phenotype of LAMs

LAMs can be distinguished from tissue-resident KCs by their distinct lipid-handling features, which emerge largely from monocyte-derived precursors[23,24]. However, the mechanisms governing the differentiation of recruited monocytes into LAMs rather than adopting a KC-like phenotype remain poorly explored. To identify potential transcription factors (TFs) regulating the expression of lipid metabolism-associated genes in LAMs, we used pySCENIC[25] to reconstruct cell-type-specific gene regulatory networks (GRNs) from our single-cell transcriptome data.

The specificity of the regulons (that is, TFs and their target genes) was quantified and ranked from high to low across different cell types separately[26]. Validating this approach, several well-established macrophage lineage TFs such as NR1H3 (ref. 27) and MAFB[28] were simultaneously identified as the most specific TFs for both LAM and KC (Fig. 3a and Extended Data Fig. 3a). Of note, a regulon regulated by the melanocyte lineage TF microphthalmia-associated transcription factor (MITF)[29] was exclusively activated in LAMs (Fig. 3b,c and Extended Data Fig. 3b), which is consistent with the LAM-specific *MITF* gene expression (Extended Data Fig. 3c), suggesting a pivotal role for MITF in the regulation of LAM differentiation. Furthermore, elevated activity of the MITF regulon was observed, particularly in LAMs from patients with MASH (Fig. 3d), correlating with their increased severity of steatosis within the hepatic microenvironment.

Gene ontology (GO) enrichment analysis of the top 100 predicted MITF target genes revealed significant enrichment for lipid-metabolism-associated processes, including low-density lipoprotein particle clearance and triglyceride (TG)-rich lipoprotein particle clearance (Fig. 3e). Among these, canonical LAM markers, including *TREM2*, *CD9* and *GPNMB*, along with genes involved in lipid transport and metabolism (for example, *FABP4*, *LPL*, *FABP5*, *DHRS9*, *MGLL* and *PLA2G7*), were identified as MITF-regulated targets and exhibited a LAM-specific expression pattern (Fig. 3f and Extended Data Fig. 3d). For instance, lipoprotein lipase (LPL), encoded by *LPL*, serves as a pivotal enzyme in TG metabolism, catalyzing the hydrolysis of TGs carried by plasma very-low-density lipoprotein and circulating chylomicrons[30].

We further confirmed the LAM-specific expression of MITF at the protein level through immunofluorescence (IF) across three disease conditions (Fig. 3g). To examine the effects of the MITF on LAM phenotype transformation, we induced *MITF*-OE in the THP-1 cell line using lentivirus transduction (Methods). As expected, *MITF*-OE in THP-1 cells led to a significant upregulation of several LAM signature genes[10], including *GPNMB*, *LPL*, *DHRS9*, *LGALS3*, *CTSD*, *PLD3* and *PLA2G7* (Fig. 3h). Conversely, *MITF* knockdown via small interfering RNA (siRNA) for 24 h resulted in downregulation of these genes (Extended Data Fig. 3e). All together, these results indicate that the MITF-regulated GRN has a critical role in determining the lipid-handling phenotype of LAMs.

MITF enhances fatty acid oxidation in LAMs via the PGC1α–PPARγ signaling axis

To deepen the understanding of how LAMs diverge from tissue-resident KCs in their roles in coordinating local lipid metabolism, differential gene expression and Kyoto Encyclopedia of Genes and Genomes (KEGG) pathway analyses were conducted between these two macrophage subtypes (Fig. 4a,b). We found enrichment for the peroxisome proliferator-activated receptor (PPAR) signaling pathway in LAMs, which is consistent with the LAM-specific activation of the PPARγ

Fig. 4 | MITF–PGC1α–PPARγ–FAO signaling axis in LAMs. a, Volcano plot displaying differently expressed genes (absolute $\log_2$(fold change) > 2.0, $P < 0.01$) between LAMs and KCs. The red and blue spots indicate genes overexpressed in LAMs and KCs, respectively. The top 30 significantly upregulated or downregulated gene names are marked. *P* values were calculated using a two-sided Wilcoxon rank-sum test and adjusted using the Benjamini–Hochberg procedure. $-\log_{10}$(FDR) was capped using computational precision limits. **b**, Top KEGG terms enriched by ORA for upregulated DEGs of LAMs, compared with KCs. *P* values were computed with a two-sided Fisher's exact test and adjusted for multiple testing using the Benjamini–Hochberg procedure. **c**, Binarized activity of the PPARγ regulon for each cell generated from the SCENIC AUC distribution displayed in the UMAP space, with the red spots representing cells that are activated. **d**, GRNs showing the predicted candidate target genes for the following TFs: MITF, PPARγ, NR1H3, MAFB, MEF2A, SPIC, RXRA, ETV5 and MAF. The line width of the edges indicates the predicted weight between the corresponding TF and its target gene. **e**, Spatial distribution of the scores of MITF regulon and PPAR signaling activity in eight randomly selected MASH biopsy sections. **f**, Expression of *PGC1A*, *PPARG*, *CPT1A*, *CPT1B*, *ACADVL* and *HADHA* using RT–qPCR in THP-1 cells after MITF-OE compared to EV ($n = 6$ biological replicates). **g**, The mitochondrial OCR of THP-1-EV and THP-1 *MITF*-OE cells was measured using an extracellular flux analyzer ($n = 3$ biological replicates). Oligomycin, carbonyl cyanide-*p*-trifluoromethoxyphenylhydrazone (FCCP) and rotenone + antimycin A were injected at the indicated time points. **h**, Representative confocal micrographs of MitoTracker Red CMXRos-stained THP-1 cells after transfection with either EV or *MITF*-OE (left). Quantification of mitochondrial fluorescence intensity is shown ($n = 3$ biological replicates, multiple regions per sample). **i**, Schematic representation of the MITF-PGC1α–PPARγ–FAO signaling axis in LAMs. Data are presented as mean values ± s.d.; statistical significance was determined using an unpaired, two-sided Student's *t*-test.

https://doi.org/10.1038/s41588-025-02407-8

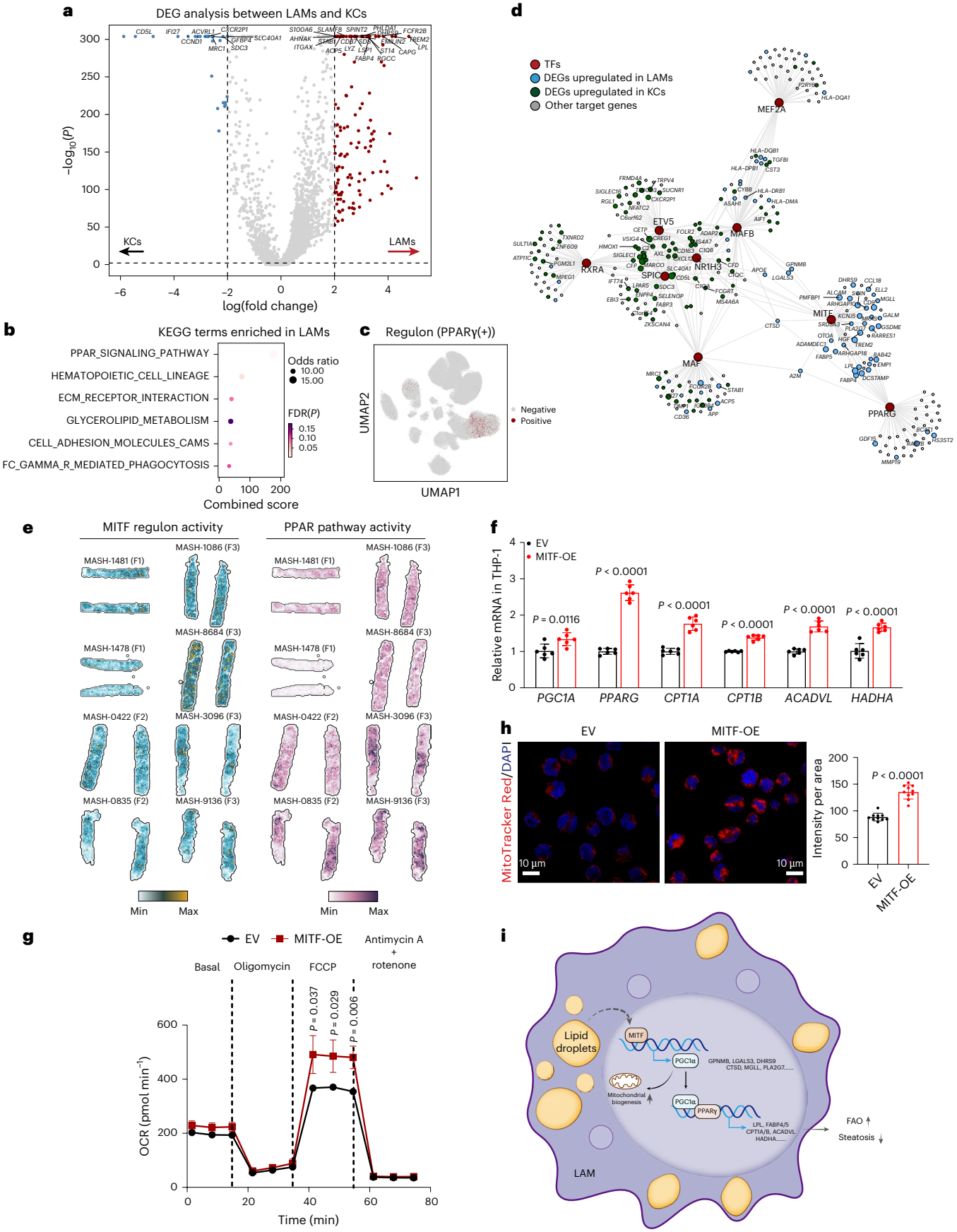

regulon (Fig. 4c and Extended Data Fig. 3f). By constructing a GRN consisting of the top five cell-type-specific regulons for both LAMs and KCs, alongside common TFs such as NR1H3, MAF, MAFB and MEF2A, we observed that differentially expressed genes (DEGs) upregulated in each cell subset were predominantly regulated by their respective key TFs: ETV5, RXRA and SPIC for KCs, and MITF and PPARγ for LAMs (Figs. 3c and 4d and Extended Data Fig. 3a). Based on these findings, it is tempting to speculate that MITF could drive the activation of the PPAR signaling pathway in LAMs.

Therefore, we scored the activity of both the MITF regulon and the PPAR signaling pathway and found a strong correlation between their spatial distribution observed in each Visium ST section from our cohort with MASLD (Fig. 4e). Consistent with this, a previous study showed that MITF directly regulates the expression of PPARγ co-activator 1α (PGC1α), which acts as a master regulator of mitochondrial biogenesis and oxidative phosphorylation[31]. Additionally, the PGC1α–PPARγ axis transactivates several genes to control lipid metabolism and induce a spike in fatty acid oxidation (FAO) to control myogenesis[32]. Supporting this, our results showed that *MITF*-OE in THP-1 cells significantly upregulated *PGC1A*, *PPARG* and several key PGC1α–PPARγ target genes involved in FAO, including *CPT1A*, *CPT1B*, *ACADVL* and *HADHA* (Fig. 4f). On the other hand, *MITF* knockdown using siRNA for 24 h resulted in significant downregulation of these genes (Extended Data Fig. 3g). Furthermore, the oxygen consumption rate (OCR), an indicator of oxidative phosphorylation, was significantly higher in *MITF*-OE THP-1 cells (Fig. 4g), probably because of increased mitochondrial mass upon *MITF*-OE (Fig. 4h). Collectively, these results underscore the central role of MITF in modulating mitochondrial function and lipid-handling capacity in LAMs, mediated by the PGC1α–PPARγ–FAO axis (Fig. 4i).

Differential intercellular flow analysis indicates a hepatoprotective role for LAMs

To capture the intercellular signaling dynamics associated with MASLD progression, we applied FlowSig[33] to the scRNA-seq data, revealing differentially inflowing and outflowing signals across the MASLD spectrum (Fig. 5a,b and Extended Data Fig. 4a,b). We constructed 30 gene expression modules (GEMs) using PyLIGER[34], which captured differences across cell types (Extended Data Fig. 4c,d). Compared to CTRLs, MASL exhibited increased inflow of interleukin-6 through leukemia inhibitory factor receptor and interleukin-6 cytokine family signal transducer, vascular endothelial growth through kinase insert domain receptor, interleukin-13 through interleukin-13 receptor subunit alpha-2, calcitonin gene-related peptide type 1 receptor and the chemokine receptor CXCR3 (Extended Data Fig. 4a), along with elevated outflow of migration inhibitory factor (originating from cholangiocytes and cDC1s), interleukin-33 (LSECs, central vein ECs and portal vein ECs) and angiopoietin-related protein 1 (cholangiocytes and HSCs) (Fig. 5c). Progression to MASH involved minimal additional inflow alterations (Extended Data Fig. 4b), but a marked amplification of outflowing mediators, notably hepatocyte growth factor (HGF) from LAMs, CXCL3 (LAMs, KCs, cholangiocytes and $CD14^+/CD16^+$ monocytes), protein Wnt-10a (plasma_IgA, plasma_IgG and pDCs) and interleukin-1A from the broader myeloid compartment (Fig. 5b–d). To reveal the regulatory architecture underlying augmented outflow signaling, we constructed global intercellular flow networks by mapping significantly upregulated inflowing signals that form directed paths toward one or more elevated outflows, along with their associated GEMs (Extended Data Fig. 4e,f).

The pronounced elevation of HGF outflow from LAMs in patients with MASH is of particular interest, as a previous study by Kroy et al.[35] demonstrated that hepatocyte-specific deletion of c-Met, the receptor for HGF, in a mouse model of MASH, resulted in an exacerbated phenotype marked by higher fatty acid accumulation and increased apoptosis[35], suggesting that LAMs have a hepatoprotective role during MASLD progression via the HGF–MET axis, most probably within hepatic crown-like structures[11,24]. To corroborate that LAMs serve as an additional critical source of HGF, alongside the well-established role of HSCs, we examined the localization of *HGF* mRNA in LAMs using RNAscope (Fig. 5e). To explore the potential impact of LAMs on hepatocyte functions, we observed that hepatocytes in proximity to LAMs exhibited a proliferative phenotype (Extended Data Fig. 4g). To investigate this further, we cultured human hepatocytes (HepG2 cells) with conditioned medium from THP-1 cells with or without *MITF*-OE. Notably, *MITF*-OE in THP-1 cells significantly increased ex vivo production of HGF (Fig. 5f) and enhanced the ability of THP-1 conditioned medium to stimulate HepG2 cell proliferation (Fig. 5g) and reduce apoptosis (Fig. 5h). Collectively, our intercellular flow analysis suggests a hepatoprotective role of LAMs via the HGF–MET axis during MASLD progression (Fig. 5i).

ST analysis with topic modeling uncovers a spatial gene topic of MASLD-associated fibrosis

To uncover MASLD-related gene signatures within a spatial context, our human MASH datasets including 16,000 Visium spots were deconvoluted into 20 'spatial topics' using ST analysis with topic modeling (STAMP)[36] (Methods and Extended Data Fig. 5a). Further examination of the distribution of spots with the highest topic activity (99th percentile) across all ST sections revealed six non-parenchymal spatial topics that were more prevalent in MASLD than in CTRLs (Fig. 6a and Extended Data Fig. 5a–c). These spatial topics corresponded to MASLD-relevant cell populations and signaling pathways. For example, Topic3 featured markers of KCs (*CD5L*, *VSIG4* and *TIMD4*), while Topic4 presented a LAM-specific gene expression module (*FABP4*, *SPP1*, *TREM2* and *LPL*).

The Topic5 profile reflects a pathological extracellular matrix/fibrogenesis pathway marked by collagen-related (*COL1A1*, *COL1A2* and *COL14A1*) and fibrosis-related (*THY1*, *LTBP2*, *LOXL1*, *MFAP4*, *ITGBL1* and *LUM*) genes[37] (Fig. 6b), which was particularly enriched in patients with MASH with fibrosis stages 3–4 (Fig. 6c). Zoom-in visual inspection confirmed that spots with high Topic5-activity spatially aligned with the histology of fibrotic foci and its activity correlated with the abundance of HSCs and central vein ECs, as inferred by cell2location[38] (Fig. 6d and Extended Data Fig. 5d), suggesting the involvement of their potential crosstalk in MASLD-related fibrogenesis.

Fig. 5 | LAMs exert hepatoprotective function via the HGF–MET axis. **a**, Differentially outflowing signals between MASL and CTRL groups. The yellow dots indicate statistically significant differential outflow (absolute $\log_2$(fold change) > 1.0, $P_{adj} < 0.01$). **b**, Differentially outflowing signals between MASH and MASL groups. The yellow dots indicate statistically significant differential outflow (absolute $\log_2$(fold change) > 1.0, $P_{adj} < 0.01$). **c**, Dot plot showing the expression patterns of differentially outflowing signals identified in both MASL versus CTRLs and MASH versus MASL. **d**, Expression of *HGF* in the myeloid compartment of the scRNA-seq dataset displayed in the UMAP space. **e**, Confocal microscopy representative images of RNAscope showing *TREM2* and *HGF* for the tissue section from the MASH group ($n = 3$ independent experiments). The white arrows denote cells double-positive for *TREM2* and *HGF*. **f**, Enzyme-linked immunosorbent assays of HGF in the conditioned medium of THP-1 EV and *MITF*-OE cells ($n = 8$ biological replicates). **g**, IF staining of Ki-67 (overlap with DAPI staining) and percentage of Ki-67^+ cells in HepG2 cells cultured with the conditioned medium described in **f** and palmitic acid for 24 h ($n = 3$ biological replicates, multiple regions per sample). **h**, Terminal deoxynucleotidyl transferase dUTP nick end labeling (TUNEL) staining (green) and percentage of $TUNEL^+$ cells in HepG2 cells cultured with the conditioned medium described in **f** and palmitic acid for 24 h ($n = 3$ biological replicates, multiple regions per sample). **i**, Schematic representation of the hepatoprotective function of LAMs via the HGF–MET axis. Data are presented as mean values ± s.d.; statistical significance was determined using an unpaired, two-sided Student's *t*-test. **i**, The illustration was created with BioRender.com.

https://doi.org/10.1038/s41588-025-02407-8

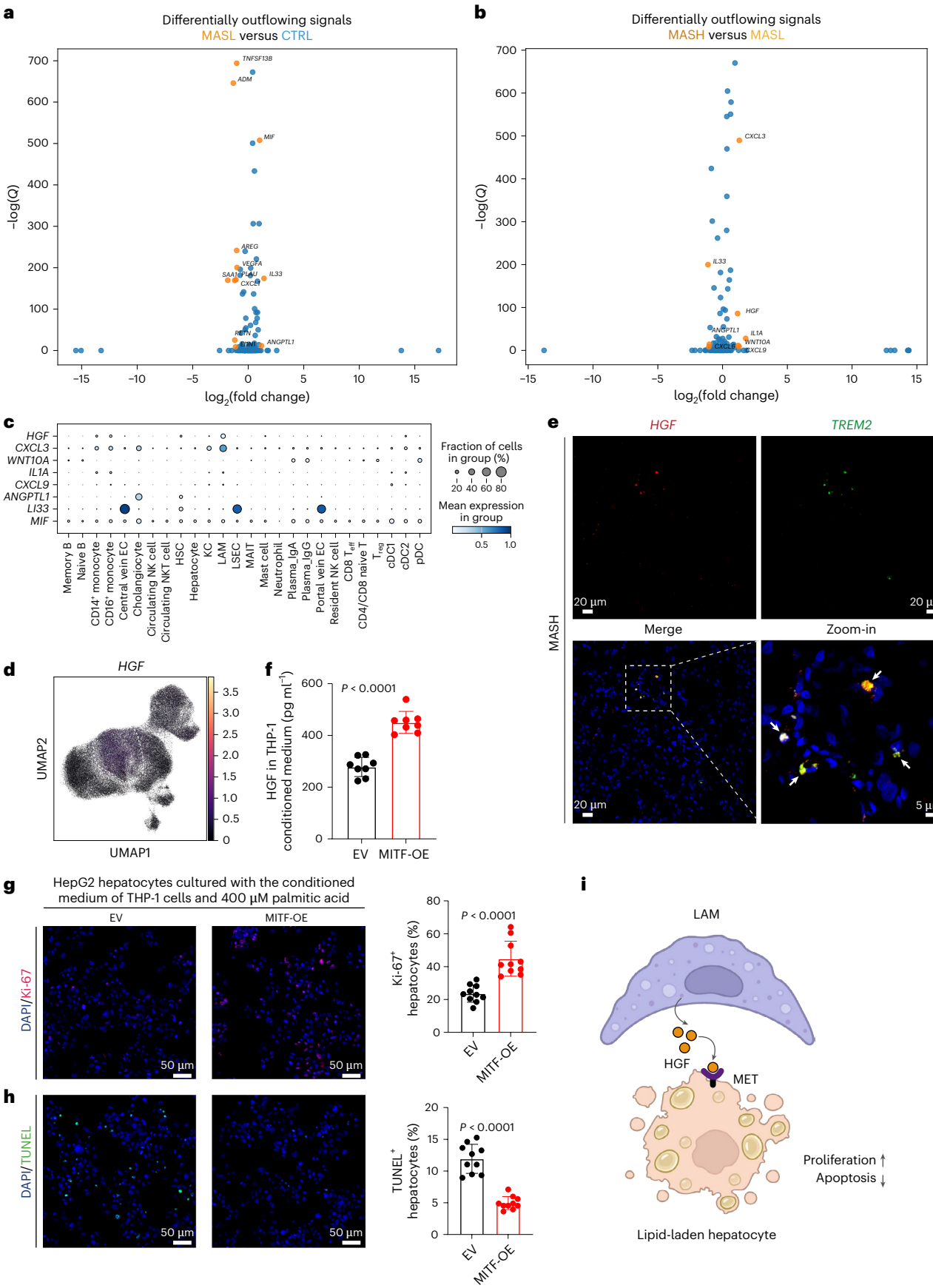

https://doi.org/10.1038/s41588-025-02407-8

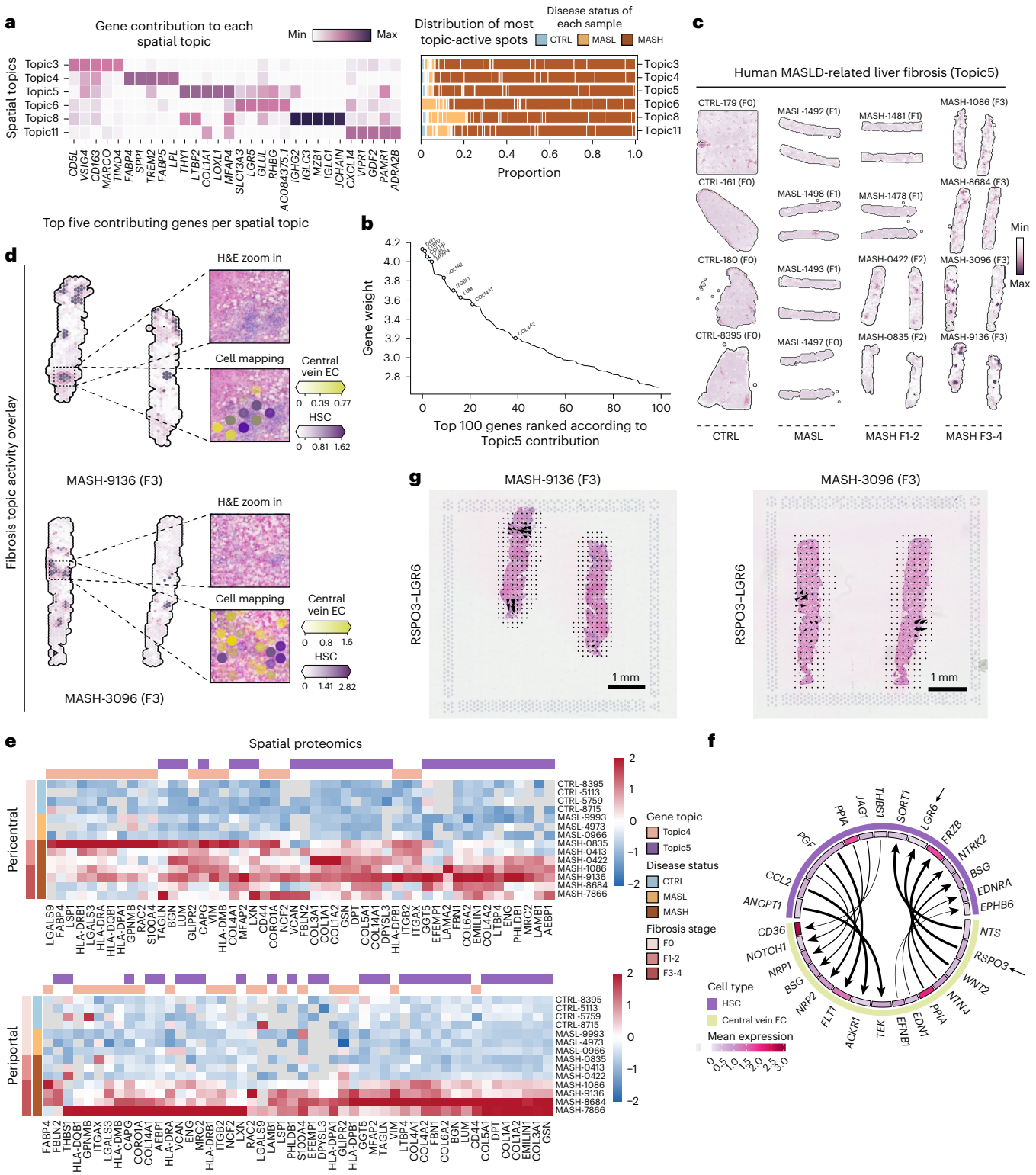

Fig. 6 | MASLD-associated fibrosis gene signatures revealed by STAMP. **a**, STAMP-identified signatures overrepresented in MASLD tissue. Their relative contribution to each spatial topic is displayed for the top five contributing genes per topic and the proportion of spots with the highest activity (99th percentile according to disease status and sample). Proportions were normalized per sample to account for differences in tissue area and total spot number. **b**, Ranking of the top 100 genes for Topic5 based on gene weight to the topic, with fibrosis-related genes emphasized. **c**, Spatial distribution of the MASLD-related liver fibrosis topic in 16 human liver tissue sections ($n = 4$ CTRL, $n = 4$ MASL, $n = 4$ MASH F1–2 and $n = 4$ MASH F3–4). **d**, Spatial distribution of the MASLD-related liver fibrosis topic in two MASH F3 tissue sections. The zoomed-in graphs display H&E images and abundance of HSCs and central vein ECs for selected fibrotic regions. **e**, Heatmap showing the expression of proteins from Topic4 and Topic5 across three disease conditions profiled using SP in ROIs from the pericentral (top) and periportal (bottom) areas. **f**, Circos plot showing significant interactions between HSCs and central vein ECs identified using CellPhoneDB. The weight of the arrows depicts the score for the interaction; the color of the bars represents the average expression of ligands and receptors for each cell type. **g**, The spatial location of the ligand–receptor pair RSPO3–LGR6 at the grid level for two representative MASH F3 biopsy samples (MASH-9136 and MASH-3096). The arrows indicate the sender signal of the RSPO3–LGR6 pair.

https://doi.org/10.1038/s41588-025-02407-8

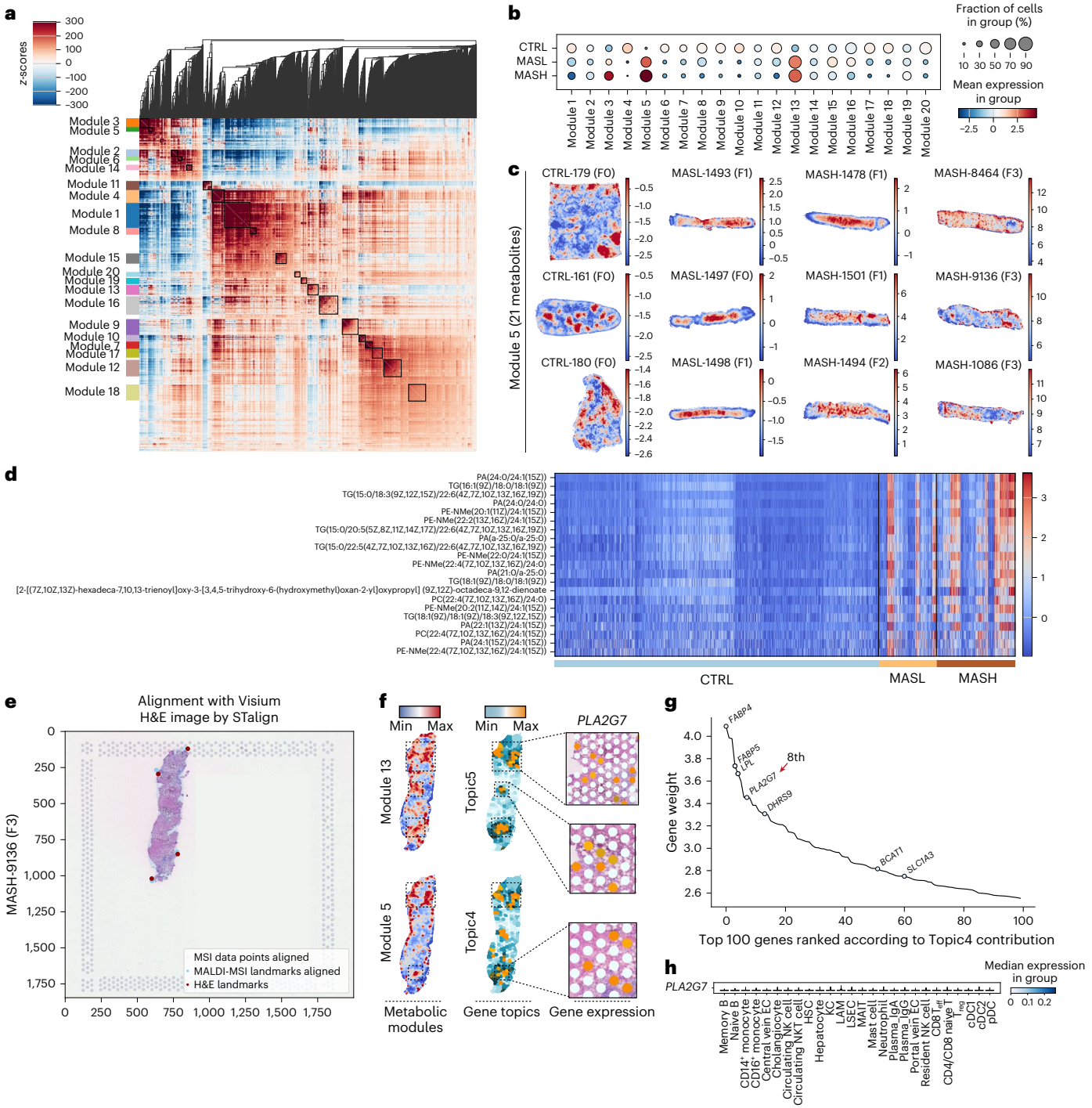

Fig. 7 | MASLD-associated metabolic modules revealed by Hotspot. **a**, Metabolites with significant spatial autocorrelation (1,528 metabolites, FDR < 0.01) were grouped into 20 Hotspot modules based on pairwise spatial correlation. **b**, Dot plot showing metabolic modules that align with disease conditions. Module expression scores were calculated using the Hotspot calculate_module_scores function, which centers metabolite expression based on a specified null model (depth-adjusted normal), smooths the value across a *k*-nearest neighbor (*k*NN) graph and then applies principal component analysis modeling using a single component. The resulting pixel loadings are reported as the module scores. **c**, Spatial distribution of Hotspot-identified module 5 in 12 representative tissue sections. **d**, Twenty-one metabolites from module 5 are presented as a heatmap, with columns representing the pixels within each disease status and the rows displaying metabolite annotations. **e**, Overlay of MSI data points and H&E image of Visium after alignment with STalign. **f**, Spatial distribution of Metabolic modules 5 and 13 (left) and gene topics 4 and 5 aligned using STalign (right). The zoomed-in graphs display *PLA2G7* expression for three selected overlayed regions. **g**, Ranking of the top 100 genes for Topic4 based on gene weight to the topic, with metabolism-related genes emphasized. **h**, Stacked violin plot showing the expression of *PLA2G7* across major cell types identified using scRNA-seq.

To determine whether elevated RNA levels resulted in concordant increases in protein, we applied high-sensitivity mass spectrometry on pathologist-defined regions of interests (ROIs) across three disease conditions ($n = 4$ CTRL, $n = 3$ MASL and $n = 7$ MASH). Two ROIs (~100 × 200 μm^2) from the pericentral and periportal areas were isolated using laser-capture microdissection from each tissue section for proteomics profiling (Supplementary Notes). Genes specific to Topic4 (including *FABP4*, *GPNMB*, *LSP1* and *LGALS3*) and Topic5

(including *TAGLN*, *LUM*, *COL1A1* and *COL1A2*) were elevated in MASH pericentral ROIs, aligning with the transcriptomic data (Fig. 6e). In contrast, few Topic4 and Topic5 genes showed appreciable upregulation in the periportal ROIs from patients with MASL and MASH with mild fibrosis (F1–2). However, in patients with MASH with advanced fibrosis (F3–4), the periportal regions displayed marked upregulation of these genes, suggesting a more extensive dysregulation as the disease progressed.

To explore the cell–cell interactions within the Topic5-active area, we implemented CellPhoneDB[39] on our scRNA-seq dataset. Notably, *RSPO3* (R-spondin 3)[16], a pro-proliferating factor from central vein ECs, was predicted to interact with *LGR6* on HSCs (Fig. 6f), potentially driving HSC proliferation and liver fibrogenesis[40]. Consistently, we observed an enrichment of the *RSPO3*–*LGR6* interaction signal in fibrotic regions of liver biopsies, particularly from patients with MASH F3–4, using communication analysis by optimal transport[41] (Fig. 6g and Extended Data Fig. 5e). Moreover, RSPO3 was highly elevated in active fibrotic lesions from patients with idiopathic pulmonary fibrosis and MASLD[42], specifically expressed in central vein ECs[43]. These data indicate the *RSPO3*–*LGR6* interaction as a candidate signaling axis potentially involved in fibrogenesis, warranting further experimental validation.

Identifying MASLD-associated metabolic programs in situ using MALDI-MSI

To elucidate the metabolic landscape of MASLD, we applied Hotspot[44] to our MALDI-MSI datasets (n = 6 CTRL, n = 9 MASL and n = 12 MASH), including 841,534 high-quality spatially indexed metabolomes. The original spatial coordinates of each MALDI-MSI SM dataset were transformed and aligned into a unified two-dimensional coordinate system, enabling integrative analysis across all SM samples (Extended Data Fig. 6a and Methods). The transformed spatial distances served as the basis for feature selection and similarity quantification. A total of 1,528 metabolites and lipids with significant spatial autocorrelation (false discovery rate (FDR) < 0.01) were identified and decomposed into 20 spatially dependent metabolic modules based on their spatial distributions (Fig. 7a). Among these, three modules (modules 3, 5 and 13) were identified as MASLD-specific, with module 5 exhibiting the strongest correlation with disease severity (Fig. 7b), suggesting its role in disease progression from healthy to MASL and from MASL to MASH. Spatial analysis revealed that module 5 metabolites are predominantly minimally produced in the pericentral region under healthy conditions but are markedly upregulated in MASLD (Figs. 1e and 7c). Validating our approach, TG species such as TG(16:1(9Z)/18:0/18:1) and TG(16:1/18:0/18:1(9Z)), previously reported as key lipid species associated with fat accumulation in MASH[45], were found in modules 5 and 13, respectively (Fig. 7d and Extended Data Fig. 6b,c).

Beyond TGs, module 5 was primarily enriched in phosphatidylethanolamine (PE), phosphatidylcholine (PC) and phosphatidic acid (PA) species containing very-long-chain fatty acids (C ≥ 22), such as PA(24:0/24:1(15Z)), PC(22:4(7Z,10Z,13Z,16Z)/24:0), PA(24:0/24:0), phosphor-(N-methyl)-ethanolamine (PE-NMe)(20:1(11Z)/24:1(15Z)) and PE-NMe(22:2(13Z,16Z)/24:1(15Z)) (Fig. 7d). These findings implicate phospholipid (PL) metabolism in MASLD pathogenesis. To integrate the MSI-based SM data with the ST data, we aligned the MSI data points directly to the corresponding H&E images of Visium ST using STalign[46] (Fig. 7e and Extended Data Fig. 6d,e). We found that MASLD-specific metabolic modules spatially aligned with the spatial gene topics of the LAM feature (Topic4) and HSC-driven fibrogenesis (Topic5) (Fig. 7f).

To deepen the link between LAM-driven lipid metabolism and MASLD-specific metabolic alterations, we extracted metabolism-associated genes from Topic4 (Fig. 7g) using STAMP analysis. Among these, we focused on *PLA2G7*, which encodes lipoprotein-associated phospholipase A_2 (lp-PLA_2), a regulator of PL metabolism that was exclusively expressed in LAMs (Fig. 7h). Lp-PLA_2 is upregulated in macrophages in response to oxidized PL stimulation, promoting lipoprotein uptake[47]. Interestingly, elevated oxidized PL levels in KCs could lead to iron deposition and subsequent KC ferroptosis, correlating with more severe histological features of fibrosis and steatohepatitis[48]. Conversely, lp-PLA_2 OE reduces lipid peroxidation levels and strongly suppress ferroptosis[49]. Therefore, the MITF-regulated expression of *PLA2G7* in LAMs (Figs. 3f,h and 4d), may confer ferroptosis resistance, thereby sustaining robust consistent lipid metabolism capacity in LAMs.

Discussion

In this study, we used single-cell RNA expression analysis of liver parenchymal and NPC types alongside ST, metabolomics and proteomics on adjacent tissue sections to generate comprehensive molecular and cellular profiles across the spectrum of MASLD. These data can be interactively explored using the Human Masld Spatial Multiomics Atlas portal.

We focused on LAMs because of their pivotal role as major cellular responders to inflammation and metabolic dysfunction during MASLD progression, as evidenced by their increased populations and enhanced presence within steatotic lesions[10,20]. We compared TFs operating in LAMs and KCs to elucidate the mechanisms driving LAM development, revealing distinct regulatory networks. Specifically, pySCENIC analysis of scRNA-seq data highlighted a skin pigmentation gene, *MITF*, as a master regulator of LAM differentiation, endowing them with enhanced lipid-handling capacity. MITF orchestrates the metabolic reprogramming of LAMs through the PGC1α–PPARγ–FAO axis. The clinical relevance of the MITF regulon is supported by prior evidence that imatinib, a PI3K/Akt inhibitor that activates MITF in monocyte-derived DCs[50], significantly ameliorates MASLD in obese mice[51]. Notably, 3 months of imatinib treatment reduced hepatic steatosis, systemic and adipose tissue inflammation, and improved insulin sensitivity. These findings highlight the therapeutic potential of manipulating LAM phenotypes and abundance either through molecular drug interventions or direct injections of bone marrow-derived macrophages[52].

The spatial gene topic of MASLD-related fibrosis spatially delineated fibrotic regions in each Visium ST section, thereby facilitating the identification of a candidate profibrotic cell–cell interaction between central vein ECs and HSCs via the RSPO3–LGR6 ligand–receptor pair, which serves as a potentially druggable target. However, HSCs may not be the sole responders to RSPO3 secreted by central vein ECs as NK-like cells have also been implicated in mediating antitumor immunity via the RSPO3–LGR6 axis, which involves NK cell biology through MYC upregulation and ribosomal biogenesis[53]. Accordingly, the clonal expansion of circulating NKT cells observed in patients with MASL and MASH in our cohort could, at least in part, be attributed to their response to RSPO3 secreted by central vein ECs. Thus, the RSPO3–LGR6 axis appears to have roles in both inflammation and fibrogenesis, presenting a promising therapeutic target.

Our SMA pipeline provided a framework to integrate the MSI-based SM and ST data profiled on adjacent tissue sections. However, it has not been applied across the entire spatially resolved multi-omics MASLD datasets because precise alignment requires a high histological similarity between tissue sections from these two spatial modalities and a time-intensive landmark selection process. Application of MASLD-associated metabolites could inform molecular pathology-based patient stratification[54], particularly for noninvasive diagnosis of MASH in patients with MASLD, where liver biopsies are necessary. Notably, the relationship between very-long-chain fatty-acid-containing PL species and lp-PLA_2-mediated LAM-driven PL metabolism remains to be elucidated.

A limitation of this study is the sex imbalance in the scRNA-seq cohort, with all control samples derived from female donors and the MASLD group consisting predominantly of male patients. Thus, we cannot fully exclude the potential influence of sex on the observed cellular

changes during disease progression. Future studies incorporating sex-balanced cohorts will be essential to delineate any sex-associated contributions to MASLD-relevant cellular programs more precisely.

In summary, these dense single-cell and spatial reference maps of the human MASLD, in conjunction with the recently developed spatiotemporal atlas of liver homeostasis and regeneration[15], and cholestatic injury and repair[16] in mouse liver, constitute a large-scale resource for generating hypotheses on chronic liver disease pathology and for further functional validation.

Online content

Any methods, additional references, Nature Portfolio reporting summaries, source data, extended data, supplementary information, acknowledgements, peer review information; details of author contributions and competing interests; and statements of data and code availability are available at https://doi.org/10.1038/s41588-025-02407-8.

References

1. Huby, T. & Gautier, E. L. Immune cell-mediated features of non-alcoholic steatohepatitis. *Nat. Rev. Immunol.* **22**, 429–443 (2022).
2. Feng, G. et al. Recompensation in cirrhosis: unravelling the evolving natural history of nonalcoholic fatty liver disease. *Nat. Rev. Gastroenterol. Hepatol.* **21**, 46–56 (2024).
3. Xiong, X. et al. Landscape of intercellular crosstalk in healthy and NASH liver revealed by single-cell secretome gene analysis. *Mol. Cell* **75**, 644–660 (2019).
4. Daemen, S. et al. Dynamic shifts in the composition of resident and recruited macrophages influence tissue remodeling in NASH. *Cell Rep.* **34**, 108626 (2021).
5. Xiao, Y. et al. Hepatocytes demarcated by EphB2 contribute to the progression of nonalcoholic steatohepatitis. *Sci. Transl. Med.* **15**, eadc9653 (2023).
6. Blériot, C. et al. A subset of Kupffer cells regulates metabolism through the expression of CD36. *Immunity* **54**, 2101–2116 (2021).
7. Friedman, S. L., Neuschwander-Tetri, B. A., Rinella, M. & Sanyal, A. J. Mechanisms of NAFLD development and therapeutic strategies. *Nat. Med.* **24**, 908–922 (2018).
8. Zhu, C., Tabas, I., Schwabe, R. F. & Pajvani, U. B. Maladaptive regeneration—the reawakening of developmental pathways in NASH and fibrosis. *Nat. Rev. Gastroenterol. Hepatol.* **18**, 131–142 (2021).
9. Guilliams, M. & Scott, C. L. Liver macrophages in health and disease. *Immunity* **55**, 1515–1529 (2022).
10. Jaitin, D. A. et al. Lipid-associated macrophages control metabolic homeostasis in a Trem2-dependent manner. *Cell* **178**, 686–698 (2019).
11. Wang, X. et al. Prolonged hypernutrition impairs TREM2-dependent efferocytosis to license chronic liver inflammation and NASH development. *Immunity* **56**, 58–77 (2023).
12. Ben-Moshe, S. & Itzkovitz, S. Spatial heterogeneity in the mammalian liver. *Nat. Rev. Gastroenterol. Hepatol.* **16**, 395–410 (2019).
13. Cunningham, R. P. & Porat-Shliom, N. Liver zonation—revisiting old questions with new technologies. *Front. Physiol.* **12**, 732929 (2021).
14. Liu, Y. et al. High-spatial-resolution multi-omics sequencing via deterministic barcoding in tissue. *Cell* **183**, 1665–1681 (2020).
15. Xu, J. et al. A spatiotemporal atlas of mouse liver homeostasis and regeneration. *Nat. Genet.* **56**, 953–969 (2024).
16. Wu, B. et al. A spatiotemporal atlas of cholestatic injury and repair in mice. *Nat. Genet.* **56**, 938–952 (2024).
17. Sun, C. et al. Spatially resolved multi-omics highlights cell-specific metabolic remodeling and interactions in gastric cancer. *Nat. Commun.* **14**, 2692 (2023).
18. Conroy, L. R. et al. Spatial metabolomics reveals glycogen as an actionable target for pulmonary fibrosis. *Nat. Commun.* **14**, 2759 (2023).
19. Vicari, M. et al. Spatial multimodal analysis of transcriptomes and metabolomes in tissues. *Nat. Biotechnol.* **42**, 1046–1050 (2024).
20. Guilliams, M. et al. Spatial proteogenomics reveals distinct and evolutionarily conserved hepatic macrophage niches. *Cell* **185**, 379–396 (2022).
21. Dann, E., Henderson, N. C., Teichmann, S. A., Morgan, M. D. & Marioni, J. C. Differential abundance testing on single-cell data using k-nearest neighbor graphs. *Nat. Biotechnol.* **40**, 245–253 (2022).
22. Edahiro, R. et al. Single-cell analyses and host genetics highlight the role of innate immune cells in COVID-19 severity. *Nat. Genet.* **55**, 753–767 (2023).
23. Xu, R. et al. Lipid-associated macrophages between aggravation and alleviation of metabolic diseases. *Trends Endocrinol. Metab.* **35**, 981–995 (2024).
24. Remmerie, A. et al. Osteopontin expression identifies a subset of recruited macrophages distinct from Kupffer cells in the fatty liver. *Immunity* **53**, 641–657 (2020).
25. Kumar, N., Mishra, B., Athar, M. & Mukhtar, S. Inference of gene regulatory network from single-cell transcriptomic data using pySCENIC. *Methods Mol. Biol.* **2328**, 171–182 (2021).
26. Suo, S. et al. Revealing the critical regulators of cell identity in the mouse cell atlas. *Cell Rep.* **25**, 1436–1445 (2018).
27. Bonnardel, J. et al. Stellate cells, hepatocytes, and endothelial cells imprint the Kupffer cell identity on monocytes colonizing the liver macrophage niche. *Immunity* **51**, 638–654 (2019).
28. Kim, H. The transcription factor MafB promotes anti-inflammatory M2 polarization and cholesterol efflux in macrophages. *Sci. Rep.* **7**, 7591 (2017).
29. Garraway, L. A. et al. Integrative genomic analyses identify MITF as a lineage survival oncogene amplified in malignant melanoma. *Nature* **436**, 117–122 (2005).
30. Yuan, C. et al. AAV-mediated hepatic LPL expression ameliorates severe hypertriglyceridemia and acute pancreatitis in Gpihbp1 deficient mice and rats. *Mol. Ther.* **32**, 59–73 (2024).
31. Haq, R. et al. Oncogenic BRAF regulates oxidative metabolism via PGC1α and MITF. *Cancer Cell* **23**, 302–315 (2013).
32. Luo, L. et al. Muscle injuries induce a prostacyclin-PPARγ/PGC1a-FAO spike that boosts regeneration. *Adv. Sci.* **10**, e2301519 (2023).
33. Almet, A. A., Tsai, Y. C., Watanabe, M. & Nie, Q. Inferring pattern-driving intercellular flows from single-cell and spatial transcriptomics. *Nat. Methods* **21**, 1806–1817 (2024).
34. Lu, L. & Welch, J. D. PyLiger: scalable single-cell multi-omic data integration in Python. *Bioinformatics* **38**, 2946–2948 (2022).
35. Kroy, D. C. et al. Hepatocyte specific deletion of c-Met leads to the development of severe non-alcoholic steatohepatitis in mice. *J. Hepatol.* **61**, 883–890 (2014).
36. Zhong, C., Ang, K. S. & Chen, J. Interpretable spatially aware dimension reduction of spatial transcriptomics with STAMP. *Nat. Methods* **21**, 2072–2083 (2024).
37. Franzén, L. et al. Mapping spatially resolved transcriptomes in human and mouse pulmonary fibrosis. *Nat. Genet.* **56**, 1725–1736 (2024).
38. Kleshchevnikov, V. et al. Cell2location maps fine-grained cell types in spatial transcriptomics. *Nat. Biotechnol.* **40**, 661–671 (2022).
39. Troulé, K., et al. CellPhoneDB v5: inferring cell–cell communication from single-cell multiomics data. *Nat. Protoc.* https://doi.org/10.1038/s41596-024-01137-1 (2025).
40. Yin, X. et al. RSPOs facilitated HSC activation and promoted hepatic fibrogenesis. *Oncotarget* **7**, 63767–63778 (2016).

41. Cang, Z. et al. Screening cell–cell communication in spatial transcriptomics via collective optimal transport. *Nat. Methods* **20**, 218–228 (2023).
42. Zhang, M. et al. Targeting the Wnt signaling pathway through R-spondin 3 identifies an anti-fibrosis treatment strategy for multiple organs. *PLoS ONE* **15**, e0229445 (2020).
43. Rocha, A. S. et al. The angiocrine factor rspondin3 is a key determinant of liver zonation. *Cell Rep.* **13**, 1757–1764 (2015).
44. DeTomaso, D. & Yosef, N. Hotspot identifies informative gene modules across modalities of single-cell genomics. *Cell Syst.* **12**, 446–456 (2021).
45. Rappez, L. et al. SpaceM reveals metabolic states of single cells. *Nat. Methods* **18**, 799–805 (2021).
46. Clifton, K. et al. STalign: alignment of spatial transcriptomics data using diffeomorphic metric mapping. *Nat. Commun.* **14**, 8123 (2023).
47. Wang, W.-Y. et al. OxLDL stimulates lipoprotein-associated phospholipase A2 expression in THP-1 monocytes via PI3K and p38 MAPK pathways. *Cardiovasc. Res.* **85**, 845–852 (2010).
48. Zhang, J. et al. Reactive oxygen species regulation by NCF1 governs ferroptosis susceptibility of Kupffer cells to MASH. *Cell Metab.* **36**, 1745–1763 (2024).
49. Oh, M. et al. The lipoprotein-associated phospholipase A2 inhibitor Darapladib sensitises cancer cells to ferroptosis by remodelling lipid metabolism. *Nat. Commun.* **14**, 5728 (2023).
50. Gutknecht, M. et al. The transcription factor MITF is a critical regulator of GPNMB expression in dendritic cells. *Cell Commun. Signal.* **13**, 19 (2015).
51. AlAsfoor, S. et al. Imatinib reduces non-alcoholic fatty liver disease in obese mice by targeting inflammatory and lipogenic pathways in macrophages and liver. *Sci. Rep.* **8**, 15331 (2018).
52. Brennan, P. N. et al. Autologous macrophage therapy for liver cirrhosis: a phase 2 open-label randomized controlled trial. *Nat. Med.* **31**, 979–987 (2025).
53. Tang, Y. et al. Tumor microenvironment-derived R-spondins enhance antitumor immunity to suppress tumor growth and sensitize for immune checkpoint blockade therapy. *Cancer Discov.* **11**, 3142–3157 (2021).
54. Zhang, X. et al. A blood-based biomarker panel for non-invasive diagnosis of metabolic dysfunction-associated steatohepatitis. *Cell Metab.* **37**, 59–68 (2025).

Publisher's note Springer Nature remains neutral with regard to jurisdictional claims in published maps and institutional affiliations.

Open Access This article is licensed under a Creative Commons Attribution-NonCommercial-NoDerivatives 4.0 International License, which permits any non-commercial use, sharing, distribution and reproduction in any medium or format, as long as you give appropriate credit to the original author(s) and the source, provide a link to the Creative Commons licence, and indicate if you modified the licensed material. You do not have permission under this licence to share adapted material derived from this article or parts of it. The images or other third party material in this article are included in the article's Creative Commons licence, unless indicated otherwise in a credit line to the material. If material is not included in the article's Creative Commons licence and your intended use is not permitted by statutory regulation or exceeds the permitted use, you will need to obtain permission directly from the copyright holder. To view a copy of this licence, visit http://creativecommons.org/licenses/by-nc-nd/4.0/.

© The Author(s) 2025

[1]Biomedical Pioneering Innovation Center (BIOPIC) and School of Life Sciences, Peking University, Beijing, China. [2]Department of Gastroenterology, The First Affiliated Hospital (Southwest Hospital), Third Military Medical University (Army Medical University), Chongqing, China. [3]Institute of Digestive Diseases of PLA, Third Military Medical University (Army Medical University), Chongqing, China. [4]Cholestatic Liver Diseases Center, The First Affiliated Hospital (Southwest Hospital), Third Military Medical University (Army Medical University), Chongqing, China. [5]Metabolic Dysfunction-Associated Steatotic Liver Disease (MASLD) Medical Research Center, The First Affiliated Hospital (Southwest Hospital), Third Military Medical University (Army Medical University), Chongqing, China. [6]Department of Gastroenterology, The Affiliated Hospital of Southwest Medical University, Luzhou, China. [7]Beijing Institute of Genomics, Chinese Academy of Sciences and China National Center for Bioinformation, Beijing, China. [8]Department of Hepatobiliary Surgery, The Second Affiliated Hospital, Third Military Medical University (Army Medical University), Chongqing, China. [9]Biomedical Pioneering Innovation Center (BIOPIC) and Academy for Advanced Interdisciplinary Studies, Peking University, Beijing, China. [10]Southampton National Institute for Health and Care Research Biomedical Research Centre, University Hospital Southampton and University of Southampton, Southampton General Hospital, Southampton, UK. [11]Metabolic Diseases Research Unit, IRCCS Sacro Cuore - Don Calabria Hospital, Negrar di Valpolicella, Italy. [12]MAFLD Research Center, Department of Hepatology, The First Affiliated Hospital of Wenzhou Medical University, Wenzhou, China. [13]Department of Internal Medicine, Section of Digestive Diseases, Yale University School of Medicine, New Haven, CT, USA. [14]Key Laboratory of Diagnosis and Treatment for the Development of Chronic Liver Disease in Zhejiang Province, Wenzhou, China. [15]State Key Laboratory of Metabolic Dysregulation & Prevention and Treatment of Esophageal Cancer, Peking-Tsinghua Center for Life Sciences, Biomedical Pioneering Innovation Center (BIOPIC), Peking University, Beijing, China. [16]Peking University Beijing-Tianjin-Hebei Biomedical Pioneering Innovation Center, Tianjin, China. [17]These authors contributed equally: Ziyu Li, Gang Luo, Changpei Gan, Huayu Zhang, Ling Li. ✉e-mail: xinshou.ouyang@yale.edu; zhengmh@wmu.edu.cn; fbai@pku.edu.cn; jin.chai@cldcsw.org

Methods

Access to human tissue and ethics oversight

This study involving human participants adhered to the ethical standards outlined in the Declaration of Helsinki (2013) and the Declaration of Istanbul (2018). The study protocol was reviewed and approved by the Ethics Committees of the First Affiliated Hospital (Southwest Hospital) of the Army Medical University (approval nos. (A)KY2021061 and (B)KY2023050)) and the First Affiliated Hospital of Wenzhou Medical University (approval no. 2016-246). Additionally, the export of human genetic information and materials received authorization from China's Ministry of Science and Technology. Before study commencement, written informed consent was obtained from all participants. Control liver samples were procured from ten patients at the Institute of Hepatobiliary Surgery of Southwest Hospital, who had no evidence of fatty liver disease, primary biliary cholangitis, autoimmune hepatitis, liver cancer, viral hepatitis or other liver diseases. Samples from patients with MASLD were obtained through biopsy procedures. The diagnosis of MASLD was based on an integration of clinical features, laboratory tests and pathological diagnosis, while excluding other known hepatic conditions. The histological characteristics of the liver samples were evaluated using the NAFLD Activity Score, which assesses steatosis, lobular inflammation and hepatocyte ballooning, along with fibrosis assessment to evaluate the severity of liver disease. The diagnosis of MASH is based on the presence of hepatocyte ballooning and lobular inflammation, along with steatosis and varying degrees of fibrosis. All histological sections were examined in blinded fashion by an experienced hepatopathologist.

Multiplex IF staining

Cellular colocalization and expression of proteins were validated using a multiplex immunohistochemistry/IF staining kit (cat. no. abs50012, Absin) according to the manufacturer's instructions. Briefly, 4-µm-thick liver paraffin sections were initially deparaffinized, followed by antigen retrieval. Subsequently, sections underwent multiple rounds of blocking, primary antibody incubation at 4 °C for 12 h, secondary antibody incubation at 37 °C for 10 min and fluorescent dye (TSA 520, 570, 620 or 650) incubation at 37 °C for 10 min. Each antibody and dye incubation step was followed by washing with Tris-EDTA buffer. Finally, nuclei were stained with DAPI for 10 min at room temperature. Fluorescence was visualized using a laser scanning confocal microscope (LSM 880, ZEISS). The antibody application details are provided in Supplementary Table 3.

Generation of stable THP-1 cell lines and RT–qPCR

To construct the lentivirus needed to infect THP-1 cells, first human MITF complementary DNA (NM-198159) was cloned into pLV-CMV-MCS-EF1-ZsGreen1-T2A-Puro. Together with PSPAX2 and PCMV-VSV-G, these three plasmids were transfected into the 293T cell line. THP-1 cells were grown in Roswell Park Memorial Institute (RPMI) 1640 basic medium with 10% FCS, 1% penicillin-streptomycin and 0.05 mM 2-mercaptoethanol at 37 °C in 5% CO_2. THP-1 cells were infected with either human MITF or EV lentivirus; stable cells were then selected for their ability to grow in the presence of puromycin (Hunan Fenghui Biotechnology Co., Ltd). Total RNA was extracted from THP-1 cells using RNAiso Plus (Takara Bio) according to the manufacturer's instructions. Complementary DNA was synthesized using the PrimeScript FAST RT Reagent Kit with gDNA Eraser (Takara Bio). RT–qPCR was performed using the TB Green Premix Ex Taq II FAST qPCR kit (Takara Bio). The primers used in this study were selected from the Harvard PrimerBank; we used *GPADH* as the reference gene for normalizing gene expression (primer sequences are described in Supplementary Table 4a).

siRNA transfection

MITF siRNAs were purchased from Sangon Biotech. Nontargeting oligonucleotides were used as the negative control. siRNAs were delivered to the THP-1 cell lines according to the manufacturer's instructions (ProteanFect Max, Nanoportal Biotech). The knockdown efficiency of target genes was evaluated using RT–qPCR 24 h after transfection (primer sequences and siRNA oligonucleotides are described in Supplementary Table 4b).

OCR assay and mitochondrial staining

THP-1 cells infected with either an EV or *MITF*-OE lentivirus were used to assess cellular OCR with the Seahorse XFp Cell Mito Stress Test Kit (cat. no. 103010-100, Agilent Technologies) according to the manufacturer's protocol. Briefly, cells were resuspended in prewarmed Seahorse assay medium and seeded at a density of 60,000 cells per 50 µl per well into Cell-Tak-coated Seahorse XFp Cell Culture Microplates. After cell attachment, 130 µl of Seahorse assay medium was added to each well and plates were incubated for 40 min in a 37 °C, non-CO_2 incubator before the assay. Basal OCR was then measured, followed by injection of oligomycin (3.5 µM), FCCP (2 µM) and rotenone/antimycin A (2.5 µM) through the hydrated probe plate. Real-time OCR (pmol O_2 min^{-1}) was measured using the Agilent Seahorse XFp Analyzer. Data were analyzed using the WAVE software. To assess the total mitochondrial mass, cells were stained with MitoTracker Red (cat. no. MB6046-1, Meilunbio) for 20 min, followed by fluorescence detection using a ZEISS LSM 880 laser scanning confocal microscope. Ten randomly selected fields per sample were captured; mean fluorescence intensity quantification was performed using ImageJ (v.1.8.0) (National Institutes of Health) with background subtraction.

RNAscope in situ hybridization

To colocalize HGF and TREM2, an RNAscope assay was performed using an RNAscope Multiplex Fluorescent Reagent Kit v2 (cat. no. 323100, Advanced Cell Diagnostics) according to the manufacturer's instructions. Briefly, 4-µm-thick liver paraffin sections were prepared and processed through deparaffinization, hydrogen peroxide treatment, target retrieval and RNAscope Protease IV treatment. Sections were then hybridized with the target probes HGF (cat. no. 310761-C2) and TREM2 (cat. no. 420491-C3) for 2 h. This was followed by sequential signal amplification using AMP1, AMP2 and AMP3 for 30 min, 30 mins and 15 min, respectively. For signal labeling in the C2 channel, sections were incubated with HRP-C2 for 15 min, followed by Opal 570 dyes for 30 min and HRP blocker for 15 min. This signal labeling procedure was then replicated for the C3 channels using Opal 520 dyes. Finally, sections were counterstained with DAPI at room temperature. After each step, sections were washed with RNAscope 1× Wash Buffer. Fluorescence was visualized using a laser scanning confocal microscope (LSM 880). The colocalization signals were analyzed using the ZEN software (v.2.3).

Conditioned medium experiment

Conditioned media were collected from the THP-1 EV or *MITF*-OE cell lines after 48 h of culture. Cells were seeded at a density of 1×10^6 cells per T75 flask containing 15 ml of RPMI 1640 basic medium (cat. no. C11875500, Thermo Fisher Scientific) supplemented with 10% FCS (cat. no. S711-001S, Lonsera). After incubation, cellular debris was removed by centrifugation at 4,000*g* for 10 min at room temperature. Human HGF concentrations in the conditioned media were quantified using a Quantikine ELISA Kit (cat. no. DHG00B, R&D Systems), according to the manufacturer's instructions.

Computational analysis

Mapping of the gene expression libraries. For the scRNA-seq data, raw reads were processed to generate gene expression profiles using Celescope (v.1.15.0) (Singleron Biotechnologies) with default parameters. Space Ranger (v.3.1.1) (https://support.10xgenomics.com) was used to preprocess the sequencing data, with the default settings for the ST data. Both types of libraries were mapped to the 10x GRCh38 reference.

scRNA-seq data processing. The scRNA-seq libraries were analyzed using the standard SCANPY (v.1.10.3)[55] workflow. We discarded (1) cells with fewer than 200 genes and fewer than 400 unique molecular identifiers (UMIs), (2) cells with more than 30% of counts mapped to ribosomal or mitochondrial genes, (3) cells with more than 1% of counts mapped to hemoglobin genes, (4) cells with more than 40,000 UMIs, (5) cells with more than 6,000 genes and (6) doublets as estimated using Scrublet[56] with default parameters. Additionally, doublet clusters, identified by observing the expression of markers from multiple cell types in scRNA-seq, were removed. Gene expression values were normalized for library size and log-transformed. Principal component analysis was carried out using the top 6,000 highly variable genes. Neighbors were identified using the first 30 principal components corrected using Harmony[57]; clustering was done using the Leiden algorithm with the ten nearest neighbors per cell. UMAP projections were calculated using default parameters.

Zonation annotation of Visium ST data. To identify groups of spots in different ST samples that shared similar gene expression patterns, we integrated and clustered the 10x Visium spots of all sections using the intersection of 14,000 spatially variable genes identified from each section after batch correction using a deep learning-based STAligner (v.1.0.0) method[58]. These groups of spots were manually annotated into four liver lobular zones (portal, periportal, mid and central) using marker genes and location information from the literature. Spot clustering was performed by first creating a spatial network using the Cal_Spatial_Net function with the following parameters: model = kNN and k_cutoff = 6. The number of clusters was constrained to four by specifying the num_cluster parameter during the execution of the mclust_R function of the STAligner package.

Spatial mapping of cell types in Visium ST using cell2location. Deconvolution of the abundance information of each cell type in each 10x Visium spot was performed with cell2location (v.0.1.3)[38]. Cell2location estimates the gene expression signatures of the cell types identified from reference scRNA-seq datasets using negative binomial regression, which accounts for batch effects. The inferred signatures are used to estimate the absolute spatial abundance of corresponding cell types across each Visium ST section separately. ST data were processed to untransformed and unnormalized mRNA counts filtered to genes shared with scRNA-seq data, while excluding mitochondrial and ribosomal genes. Hyperparameters in the cell mapping step based on tissue feature and experiment quality are as follows: (1) expected cell abundance per location = 8 and (2) regularization of within-experiment variation in RNA detection sensitivity = 20. The model achieved convergence after 30,000 iterations. Evidence lower bound loss function scaling according to locations × genes was used. Results were visualized according to the cell2location tutorial.

Differential abundance analysis. We used miloR[21] (v.2.0.0) to test for the differential abundance of cells within defined neighborhoods between two conditions (that is, MASL/MASH versus CTRLs or MASH versus MASL). We first used the buildGraph function to construct a *k*NN graph with the following parameters: $k = 30$, $d = 30$ and reduced.dim = X_pca_harmony. Next, we used the makeneighborhoods function to assign cells to neighborhoods based on their connectivity over the *k*NN graph. For computational efficiency, we subsampled 10% of T and NK cells and monocytes and DCs and 30% of B lineage cells, respectively. The testNhoods function was used to conduct the differential neighborhood abundance testing over samples with the scRNA-seq library (that is, collected after the first or second centrifugation step) as the covariate. To control for multiple testing, we adapted the spatial FDR implemented in Milo and used a 0.05 spatial FDR as the threshold for significance. The spatial FDR and $\log_2$(fold change) of the number of cells between two conditions in each neighborhood were used for visualization.

TCR and BCR analysis from scVDJ-seq. Droplet-based sequence data for the scTCR and scBCR sequences were aligned and quantified using Celescope multi_flv_CR against the GRCh38 human VDJ reference genome. Filtered annotated contigs were analyzed using Scirpy[59] (v.0.19.1). For the scTCR analysis, we selected T cells that were annotated as the following five cell types via the scRNA-seq analysis: MAIT cells, T_{reg}, circulating NKT cells, CD4/CD8 naive T cells and CD8 T_{eff} cells. Only T cells with both TCR-α (TRA) and TCR-β (TRB) chains were kept for further analysis. Each unique TRA–TRB pair was defined as a clonotype. The scBCR analysis was conducted on cells that were annotated as the following four cell types using the scRNA-seq analysis: naive B, memory B, Plasma_IgG and Plasma_IgA. Only B cells with both heavy (IGH) and light (IGL or IGK) chains remained for the downstream analysis. Each unique IGH–IGL/IGK pair was defined as a clonotype. For the TCR data, clonotype clusters were defined based on CDR3 amino acid sequences with receptor_arms = 'all', dual_ir = 'any' and a default cutoff of ten. For the BCR data, the cutoff parameter of the clonotype_network function used for calling clonotype clusters was set to five, with other parameters remaining the same as in the TCR analysis.

Analysis of GRNs. The SCENIC workflow[60,61] (pySCENIC v.0.12.1) was used to predict TFs and their target genes regulated from our scRNA-seq dataset. We set the broad cell type as the group identity and downsampled 5% of cells from each identity because of the limitation of the computing resources. Gene regulatory interactions for 30,499 genes were calculated based on coexpression across the scRNA-seq datasets with GRNBoost2 (ref. 62) (arboreto_with_multiprocessing–method grnboost2). This was followed by pruning interactions, which involved incorporating established TF binding motifs and constructing dataset-specific regulatory regulons[63] (pyscenic ctx–mask_dropouts). With the dropout masking set to True, the correlation between a TF and its target genes was calculated using only cells with nonzero expression values during regulon creation. Additionally, as input, we used the curated list of 1,390 human-specific TFs (https://raw.githubusercontent.com/aertslab/pySCENIC/master/resources/hs_hgnc_curated_tfs.txt), an annotation file for motif to TF mapping (https://resources.aertslab.org/cistarget/motif2tf/motifs-v9-nr.hgnc-m0.001-o0.0.tbl) (human, v9, mc9nr) and the ranking database of regulatory features (https://resources.aertslab.org/cistarget/databases/homo_sapiens/hg38/refseq_r80/mc9nr/gene_based/hg38__refseq-r80__500bp_up_and_100bp_down_tss.mc9nr.genes_vs_motifs.rankings.feather) (hg38, mc9nr, +500 bp and −100 bp transcription start site). Then, the activity of regulons was inferred for each cell using AUCell (pyscenic aucell with default parameters). The RSS was calculated for each cell type separately. The differentially activated TF regulon analysis was conducted using a Wilcoxon rank-sum test. The final network was constructed with igraph (v.2.0.3) (https://CRAN.R-project.org/package=igraph), integrating node and edge attributions according to the scRNA-seq data and visualized using ggraph (v.2.1.0).

Identifying differentially flowing signal variables. When inferring intercellular flows from unique ligand–receptor interactions identified using the CellChat (v.2.1.2)[64] analysis, we used FlowSig[33] (v.0.1.2) to prioritize the informative outflowing and inflowing signal variables. Differentially inflowing and outflowing variables were identified using two separate Mann–Whitney *U* and Wilcoxon rank-sum tests. Variables were considered significant if they met the criteria of $P_{adj} < 0.01$ and an absolute log(fold change) > 1.0.

Differential expression and gene set enrichment analysis. Differential gene expression was performed using the rank_genes_groups function of Scanpy with the following parameters: tie_correct = 'TRUE'

and method = 'wilcoxon'. To reveal the function of upregulated DEGs or to assign them to biological terms, we used the get_ora_df function with the default parameters of decoupler (v.1.6.0)[65].

Cell–cell interaction analysis. The interactions between cell populations identified in our scRNA-seq dataset were identified using CellPhoneDB (v.5.0.0)[39]. First, we retrieved the interacting pairs of ligands and receptors, which met the criteria that all members were expressed in at least 10% of cells within relevant clusters. Then, to identify the most relevant interactions between cell types, we randomly permuted the cluster labels of all cells 1,000 times and determined the mean of the average receptor expression level in a cluster and the average ligand expression level in the interacting cluster, generating a null distribution for each ligand–receptor pair in each pairwise comparison between two cell types. By calculating the proportion of the means, which are equal to or higher than the actual mean, we obtained a P value for the likelihood of cell-type specificity of a given receptor–ligand complex. Only ligand–receptor pairs with $P \leq 0.01$ were visualized using CCplotR (v.0.99.3)[66]. Communication analysis of ST datasets was performed using COMMOT (v.0.0.3)[41] with default parameters.

Disease-associated spatial gene module analysis. Deconvolution through topic modeling was applied to the 10x Visium gene expression using sctm (v.0.1.3)[36]. The human MASH dataset was deconvolved into 20 spatial topics using the STAMP function with the following parameters: mode = 'sign', dropout = 0.1, n_layers = 1, gene_likelihood = 'nb' using the 4,000 most variable genes. To quantify the activity of each spatial topic, the top 100 contributing genes for each topic were used to evaluate topic-specific scores. The distribution of each topic in the human samples (CTRL, MASL and MASH) was assessed by calculating the frequency of spots in the 99th percentile of topic activity versus the total number of spots across all tissue sections.

MALDI-MSI data analysis. Raw MALDI-MSI data files were processed into a tabular format as .CSV using the pyimzML tool (https://github.com/alexandrovteam/pyimzML); files were further transformed into individual anndata objects compatible with the ST analysis pipeline based on SCANPY[55]. Pixels with fewer than 700 metabolites or fewer than 40,000 counts were excluded from the downstream analysis, as well as metabolites expressed in more than 95% of pixels. Each metabolite feature was normalized on the total ion count within individual MSI data points. All 27 individual MSI-based anndata objects were integrated into a combined anndata containing 841,534 pixels, with the original spatial coordinates of each dataset staggered to differentiate the samples. To reveal disease-associated spatial metabolite expression patterns, we applied the Hotspot (v.1.1.1)[44] analysis framework to the merged anndata object. First, an unweighted kNN graph was constructed with the six nearest neighbors (a hyperparameter) of each MSI data point in the two-dimensional space using the create_knn_graph function. Next, pairwise evaluation was performed between the post-filtered 1,528 metabolites detected using MALDI-MSI to construct a scoring matrix based on coexpression between nearby spots using the compute_local_correlations function. Finally, an agglomerative clustering procedure was applied to group metabolites with similar spatial expression patterns into modules. This began with every module represented by a single metabolite and proceeded by merging individual modules with the highest pairwise z-scores. Merging was restricted if the FDR-adjusted P between two branches exceeded 0.01 or if either branch contained fewer than 20 metabolites.

Spatial alignment of MALDI-MSI to the Visium ST data. To spatially align MALDI-MSI to the Visium data, we used STalign (v.1.0)[46]. A rasterized density image was created from the positions of the MALDI-MSI data points and served as the source image. Before alignment, MSI data points located outside the tissue sections were identified based on the marked expression of Hotspot-identified module 11 and subsequently removed. The source image was first aligned to the corresponding target H&E image of Visium ST based on four manually assigned landmark points through affine transformation. The alignment was further optimized using a large deformation diffeomorphic metric mapping framework[67]. Once the MSI data were aligned with the RNA data, we selected the nearest Visium spot for the MSI data.

Statistics and reproducibility

No statistical method was used to predetermine sample size. No data were excluded from the analyses. All in vitro experiments were repeated independently at least three times. The investigators were not blinded to allocation during the experiments and outcome assessment. Experimental data were analyzed and visualized using Prism (v.10.4.2) (GraphPad Software). All quantitative data are presented as mean values ± s.d.; statistical significance was determined using an unpaired two-sided Student's t-test.

Reporting summary

Further information on research design is available in the Nature Portfolio Reporting Summary linked to this article.

Data availability

All raw data for scRNA-seq and 10x Visium generated in this study are deposited in the Genome Sequence Archive[68] at the National Genomics Data Center[69], the National Center for Bioinformation/Beijing Institute of Genomics and the Chinese Academy of Sciences (GSA for Human: HRA007511), which are available at https://ngdc.cncb.ac.cn/gsa-human. The spatial metabolomic data have been deposited in the OMIX, the China National Center for Bioinformation/Beijing Institute of Genomics and the Chinese Academy of Sciences under accession no. OMIX009098 (https://ngdc.cncb.ac.cn/omix). The processed scRNA-seq and Visium ST data are available from OMIX under accession no. OMIX010136. The spatial proteomic data is also available from OMIX under accession no. OMIX009117. All processed data can be visualized and downloaded at the HMSMA website (https://db.genomics.cn/stomics/hmsma). Source data are provided with this paper.

Code availability

The code required to reproduce the analyses in this paper is available through GitHub at https://github.com/OMIC-coding/Spatial_multiomics_analysis_MASLD and Zenodo (https://doi.org/10.5281/zenodo.17192831)[70].

References

55. Wolf, F. A., Angerer, P. & Theis, F. J. SCANPY: large-scale single-cell gene expression data analysis. *Genome Biol.* **19**, 15 (2018).
56. Wolock, S. L., Lopez, R. & Klein, A. M. Scrublet: computational identification of cell doublets in single-cell transcriptomic data. *Cell Syst.* **8**, 281–291 (2019).
57. Korsunsky, I. et al. Fast, sensitive and accurate integration of single-cell data with Harmony. *Nat. Methods* **16**, 1289–1296 (2019).
58. Zhou, X., Dong, K. & Zhang, S. Integrating spatial transcriptomics data across different conditions, technologies and developmental stages. *Nat. Comput. Sci.* **3**, 894–906 (2023).
59. Sturm, G. et al. Scirpy: a Scanpy extension for analyzing single-cell T-cell receptor-sequencing data. *Bioinformatics* **36**, 4817–4818 (2020).
60. Aibar, S. et al. SCENIC: single-cell regulatory network inference and clustering. *Nat. Methods* **14**, 1083–1086 (2017).
61. Van de Sande, B. et al. A scalable SCENIC workflow for single-cell gene regulatory network analysis. *Nat. Protoc.* **15**, 2247–2276 (2020).
62. Moerman, T. et al. GRNBoost2 and Arboreto: efficient and scalable inference of gene regulatory networks. *Bioinformatics* **35**, 2159–2161 (2019).

63. Imrichová, H., Hulselmans, G., Atak, Z. K., Potier, D. & Aerts, S. i-cisTarget 2015 update: generalized *cis*-regulatory enrichment analysis in human, mouse and fly. *Nucleic Acids Res.* **43**, W57–W64 (2015).
64. Jin, S. et al. Inference and analysis of cell–cell communication using CellChat. *Nat. Commun.* **12**, 1088 (2021).
65. Badia-I-Mompel, P. et al. decoupleR: ensemble of computational methods to infer biological activities from omics data. *Bioinform. Adv.* **2**, vbac016 (2022).
66. Ennis, S., Ó Broin, P. & Szegezdi, E. CCPlotR: an R package for the visualization of cell–cell interactions. *Bioinform. Adv.* **3**, vbad130 (2023).
67. Glaunès, J., Qiu, A., Miller, M. I. & Younes, L. Large deformation diffeomorphic metric curve mapping. *Int. J. Comput. Vis.* **80**, 317–336 (2008).
68. Chen, T. et al. The Genome Sequence Archive family: toward explosive data growth and diverse data types. *Genomics Proteomics Bioinformatics* **19**, 578–583 (2021).
69. Bai, X. et al. Database Resources of the National Genomics Data Center, China National Center for Bioinformation in 2024. *Nucleic Acids Res.* **52**, D18–D32 (2024).
70. Li, Z. Code for major analyses in "Spatially resolved multi-omics of human metabolic dysfunction-associated steatotic liver disease". *Zenodo* https://doi.org/10.5281/zenodo.17192831 (2025).

Acknowledgements

This study was supported by the National Natural Science Foundation of China (grant nos. 82325008 and 92268110 to J.C.; grant nos. 82241230 and 82341007 to F.B.), the National Key Research and Development Program of China (grant no. 2022YFC2504602 to F.B.), the National Science Fund for Distinguished Young Scholars (grant no. T2125002 to F.B.), the Noncommunicable Chronic Diseases-National Science and Technology Major Project (grant no. 2024ZD0531300 to J.C. and Q.P.), the Project of Chongqing University Innovation Research Group/Outstanding Medical Research Group (grant nos. 2021cqspt01 and 414Z381 to J.C.), the Beijing Natural Science Foundation (grant no. Z220014 to F.B.), the New Cornerstone Science Foundation through the XPLORER PRIZE to F.B., and the National Institute of Diabetes and Digestive and Kidney Diseases of the National Institutes of Health (grant no. R01DK134549 to X.O.). This work was also supported in part by the Southampton National Institute for Health Research Biomedical Research Centre (grant no. NIHR203319 to C.D.B.).

Author contributions

J.C. conceived and designed the project with F.B., M.-H.Z. and X.O. X.-Z.J., W.X. and M.-H.Z. collected the human samples and clinical information. Z.-Y.L. performed the bioinformatic analyses. G.L., C.G., H.Z. and L.L. performed the experiments. Z.-Y.L., X.Z., G.L., C.G., L.L., X.X., S.H., X.T., J.D., L.Z., Y.P., Z.X. and Q.P. discussed and interpreted the data. Z.-Y.L. drafted the manuscript with help from M.-H.Z., F.B., J.C., X.O., G.T. and C.D.B. All authors read and approved the final manuscript.

Competing interests

The authors declare no competing interests.

Additional information

Extended data is available for this paper at https://doi.org/10.1038/s41588-025-02407-8.

Supplementary information The online version contains supplementary material available at https://doi.org/10.1038/s41588-025-02407-8.

Correspondence and requests for materials should be addressed to Xinshou Ouyang, Ming-Hua Zheng, Fan Bai or Jin Chai.

Peer review information *Nature Genetics* thanks Ping Chen, Prakash Ramachandran, and the other, anonymous, reviewer(s) for their contribution to the peer review of this work. Peer reviewer reports are available.

Reprints and permissions information is available at www.nature.com/reprints.

https://doi.org/10.1038/s41588-025-02407-8

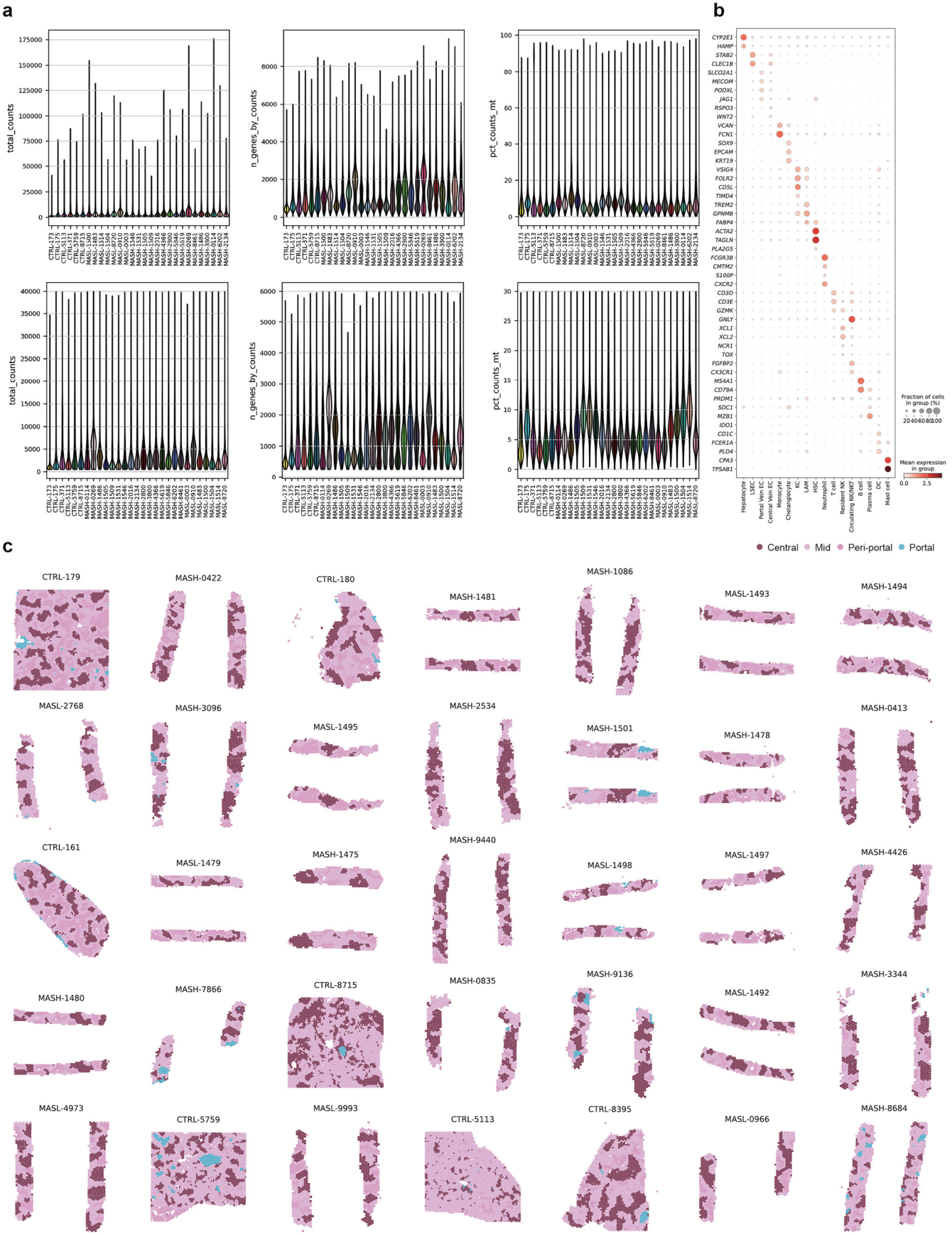

Extended Data Fig. 1 | See next page for caption.

https://doi.org/10.1038/s41588-025-02407-8

Extended Data Fig. 1 | scRNA-seq data quality control and zonation annotation for Visium ST data. a, Violin plots summarizing the number of UMIs detected per cell (total_counts), detected genes per cell (n_genes_by_counts) and the proportion of reads incident to mitochondrial genes (pct_counts_mt) per sample before (top) and after (bottom) filtering low-quality cells. **b**, Dot plots summarizing the known markers used to identify cell types. Each column corresponds to a specific cell subcluster and rows correspond to a list of key marker genes (expression normalized per gene), brackets on the right side of each plot detail the cell type or subcluster that these genes mark. **c**, Spatial distribution of four lobule zones (portal, peri-portal, mid and central) across all 35 Visium sections.

https://doi.org/10.1038/s41588-025-02407-8

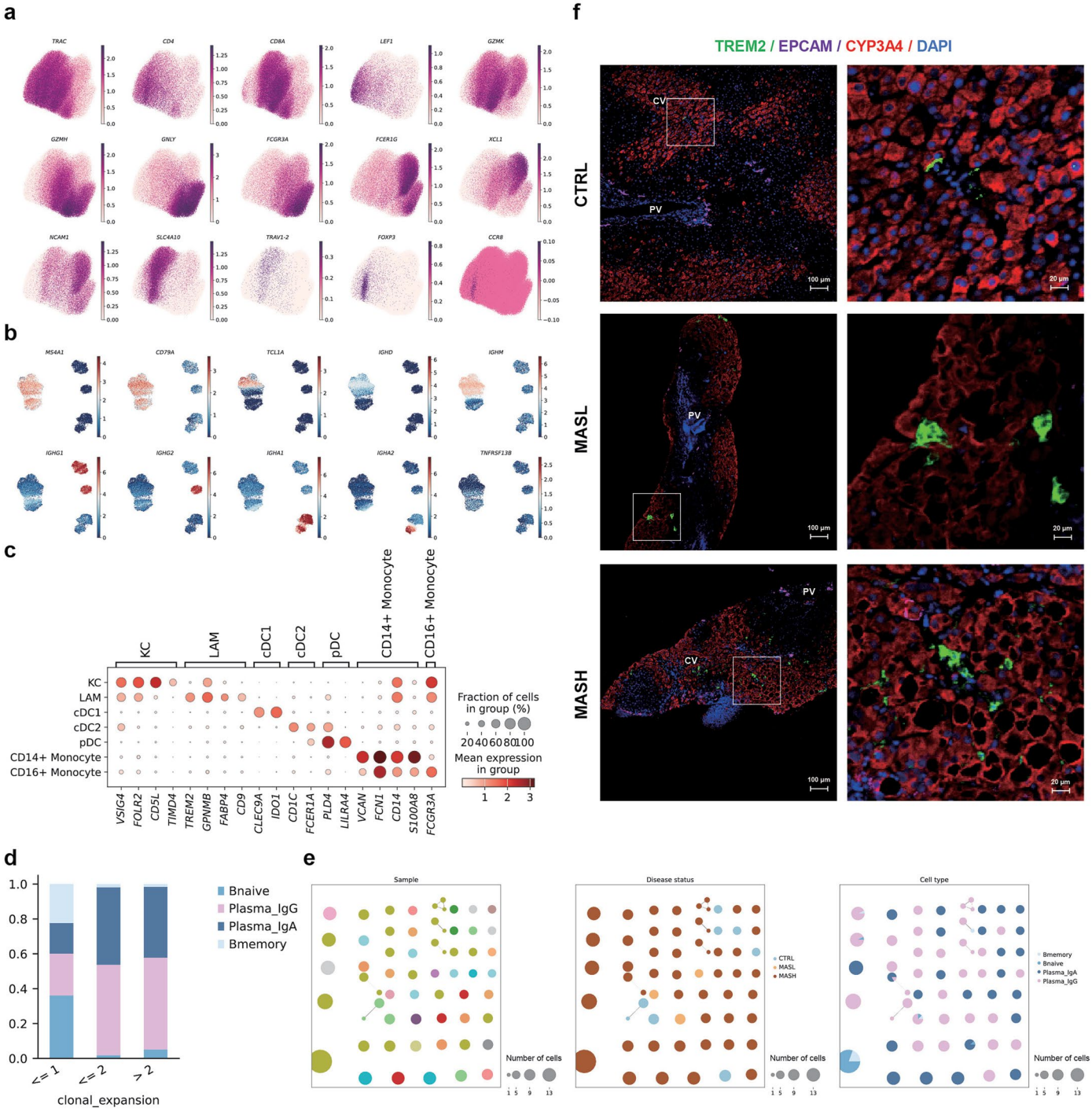

Extended Data Fig. 2 | Major cellular groups identified in the scRNA-seq datasets. a, UMAP representations colored by the expression of the known markers used to distinguish each subcluster for the T/NK compartment. **b**, UMAP representations colored by the expression of the known markers used to distinguish each subcluster for the B lymphocyte compartment. **c**, Dot plots summarizing the known markers used to distinguish each subcluster for the myeloid compartment. Each row corresponds to a specific cell subcluster and columns correspond to a list of key marker genes (expression normalized per gene), brackets on the top detail the cell type or subcluster that these genes mark. **d**, Number of B lineage cells with different clonal expansion types from the analysis of VDJ amplified libraries. **e**, Network plots showing similarity of CDR3 amino acid sequence in BCR heavy and light chain for each sample, disease status and cell type. Clonotype clusters with clonal size ≥5 are selected. **f**, Representative immunofluorescence protein staining of TREM2, EPCAM, and CYP3A4 for tissue specimens from CTRL, MASL, and MASH groups, showing the enrichment of LAMs in the pericentral area ($n = 3$, independent experiments). Scale bars, 100 µm and 20 µm (zoom-in).

https://doi.org/10.1038/s41588-025-02407-8

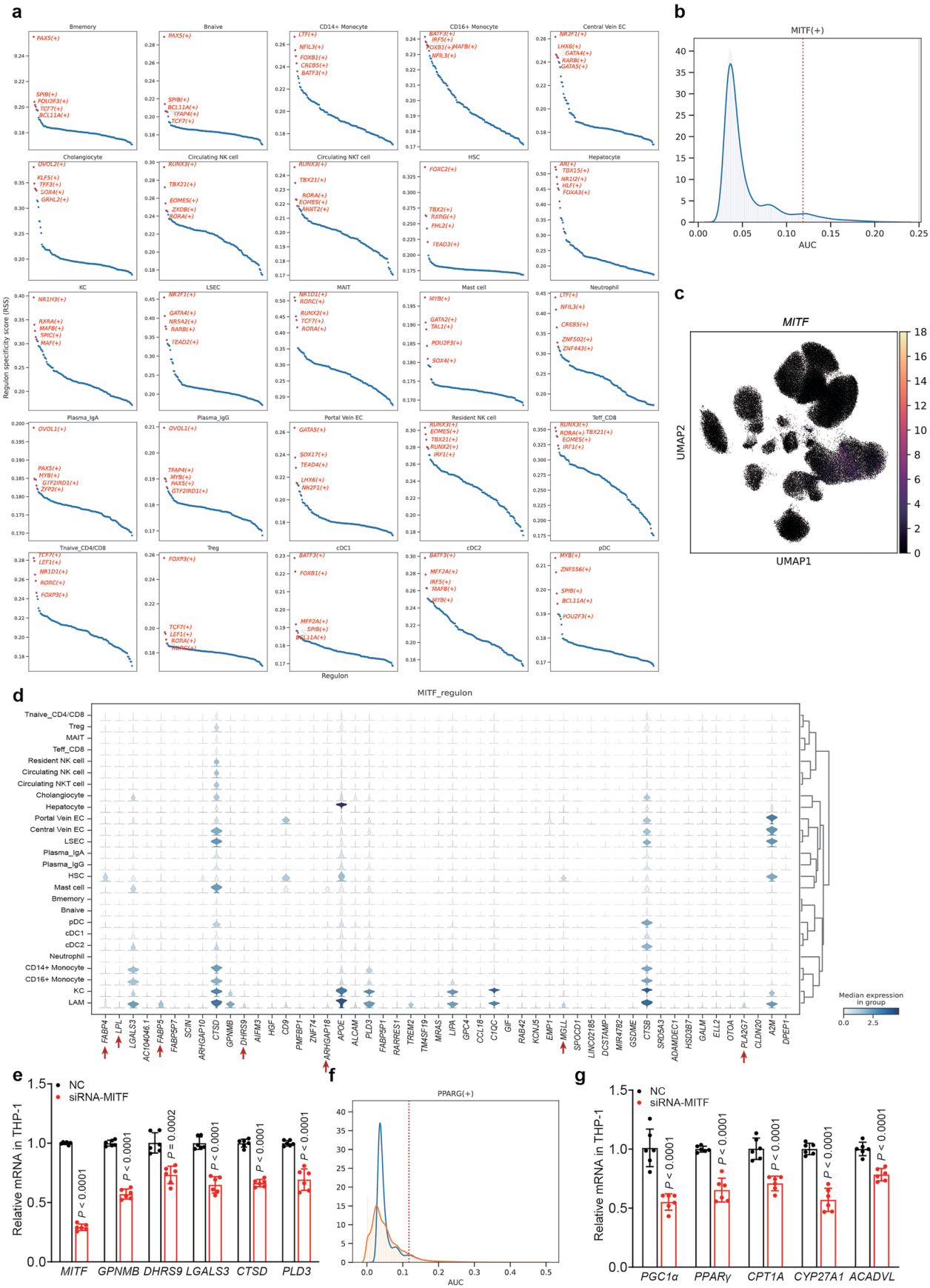

Extended Data Fig. 3 | See next page for caption.

https://doi.org/10.1038/s41588-025-02407-8

Extended Data Fig. 3 | Cell-type-specific regulons in the scRNA-seq datasets. **a**, Regulon specificity score for each annotated cell population. The top five regulons in each cell type are highlighted in red and labeled on the plot. The specificity score is shown on the Y axis. **b**, AUC distribution across cells for the MITF regulon. The calculated binary threshold is shown as a red dotted line. **c**, Expression of *MITF* gene in scRNA-seq dataset displayed in UMAP space. **d**, Stacked violin plot displaying the top 50 putative MITF-targeted gene expression levels in each cell subset, ordered by descending regulation weight. Red arrows indicate LAM-specific genes. **e**, Quantification of marker genes of LAMs by RT-qPCR in THP-1 cells after *MITF* knockdown (si-MITF) by small interfering RNA for 24 h ($n = 6$, biological replicates). **f**, AUC distribution across cells for PPARG regulon. The calculated binary threshold is shown as a red dotted line. **g**, Quantification of *PGC1α*, *PPARγ*, *CPT1A*, *ACADVL* and *CYP21A1* by RT-qPCR in THP-1 cells after si-MITF for 24 h ($n = 6$, biological replicates). Data are presented as mean values ± s.d., statistical significance was determined by unpaired two-sided Student's *t*-test.

https://doi.org/10.1038/s41588-025-02407-8

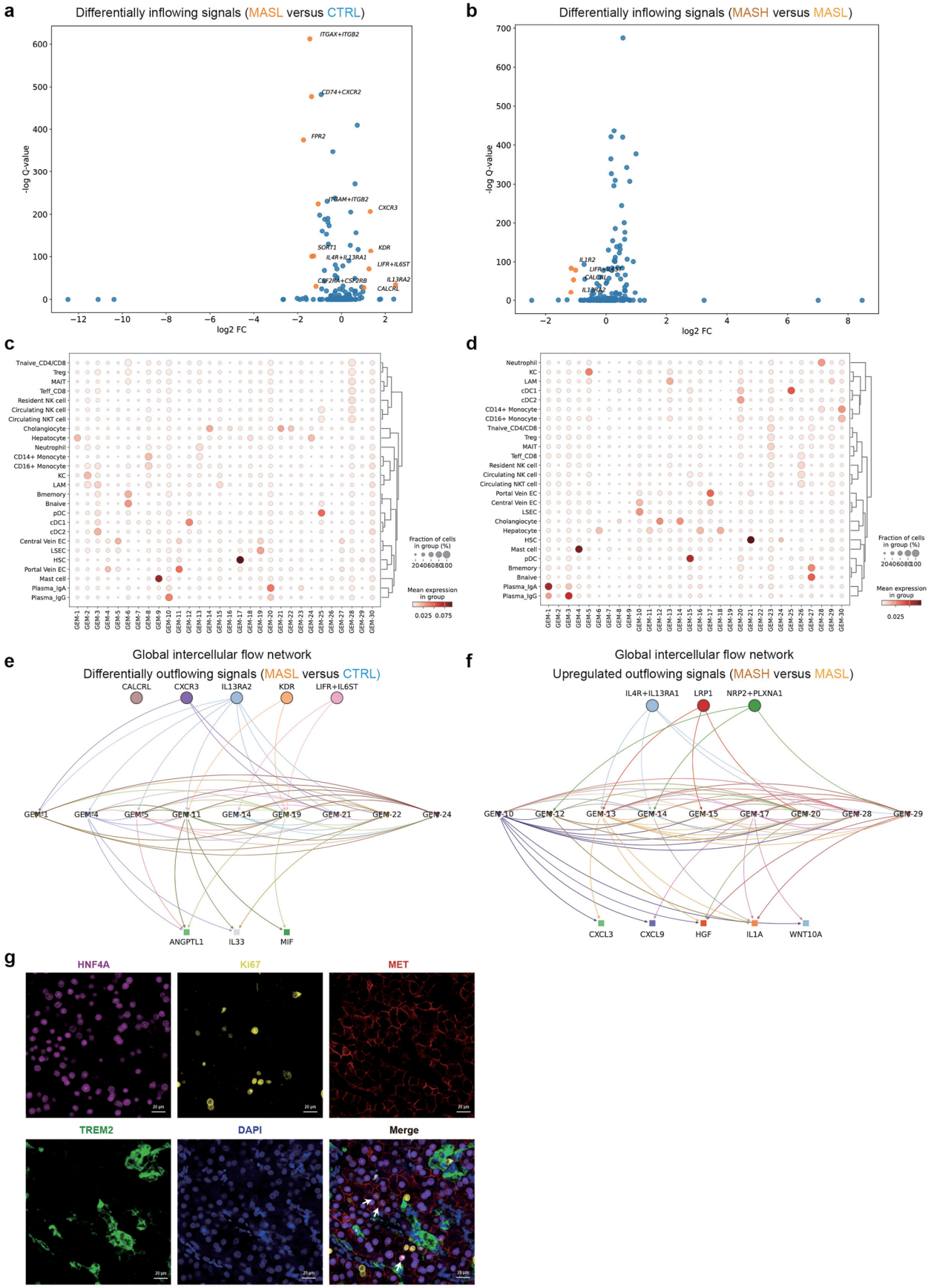

Extended Data Fig. 4 | See next page for caption.

https://doi.org/10.1038/s41588-025-02407-8

Extended Data Fig. 4 | Differential intercellular flow analysis by Flowsig. **a**, Differentially inflowing signals between MASL and CTRL groups. Yellow dots indicate statistically significant differential inflow (absolute log2FC > 1.0, adjusted *P* value < 0.01). **b**, Differentially inflowing signals between MASH and MASL groups. Yellow dots indicate statistically significant differential inflow (absolute log2FC > 1.0, adjusted *P* value < 0.01). **c**, pyLIGER-identified 30 GEMs from CTRL and MASL datasets align with cell types. **d**, pyLIGER-identified 30 GEMs from MASL and MASH datasets align with cell types. **e**, Intercellular flows regulating outflowing signals upregulated in MASL compared to CTRL. **f**, Intercellular flows regulating outflowing signals upregulated in MASH compared to MASL. **g**, Representative immunofluorescence protein staining of MET, Ki67, TREM2 and HNF4A for tissue sections from the MASH group ($n = 3$, independent experiments). Arrows indicate proliferating hepatocytes in proximity to LAMs. Scale bar, 20 μm.

https://doi.org/10.1038/s41588-025-02407-8

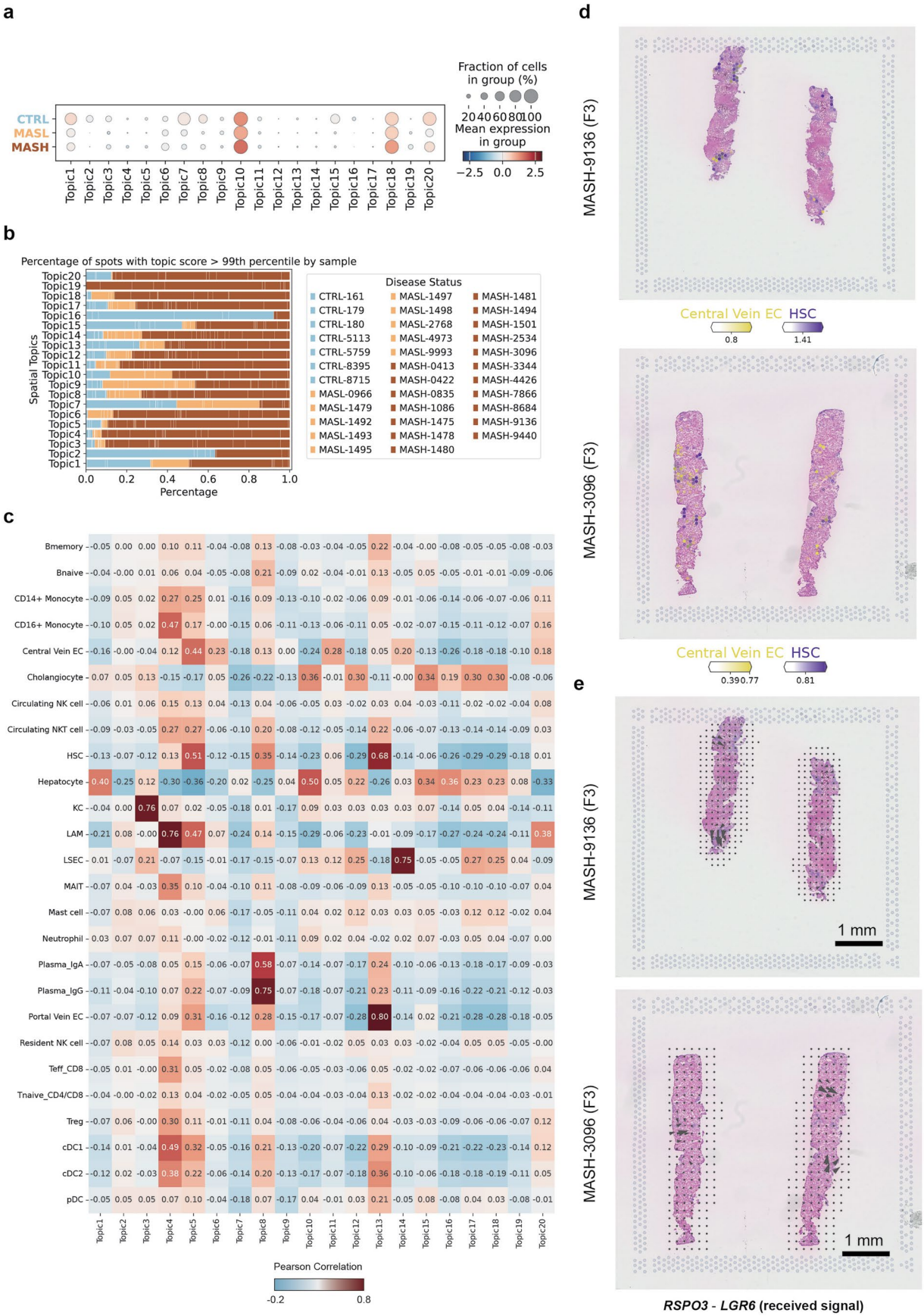

Extended Data Fig. 5 | See next page for caption.

https://doi.org/10.1038/s41588-025-02407-8

Extended Data Fig. 5 | Deconvolution of spatial gene topics in healthy and MASLD human liver. a, STAMP-identified spatial topics align with three disease conditions. **b**, Spots with the highest activity (99th percentile, T^{hi}) for each spatial topic were identified and used to calculate the proportion of T^{hi} spots among all spots, grouped by samples, colored by disease status and displayed as a stacked bar chart. **c**, Correlation (Pearson) heatmap between activities of STAMP-identified spatial topics and densities of cell2location-inferred cell types within spatial spots (strong correlation indicates spatial co-occurrence). **d**, Estimated cell abundance (color intensity) of HSCs and Central Vein ECs overlaid on H&E images for two MASH F3 stage biopsies (MASH-9136 and MASH-3096). **e**, The spatial location of the ligand-receptor pair, *RSPO3-LGR6* at the grid level for two representative MASH F3 stage biopsies (MASH-9136 and MASH-3096). The arrows indicate the receiver signal of the *RSPO3-LGR6* pair.

https://doi.org/10.1038/s41588-025-02407-8

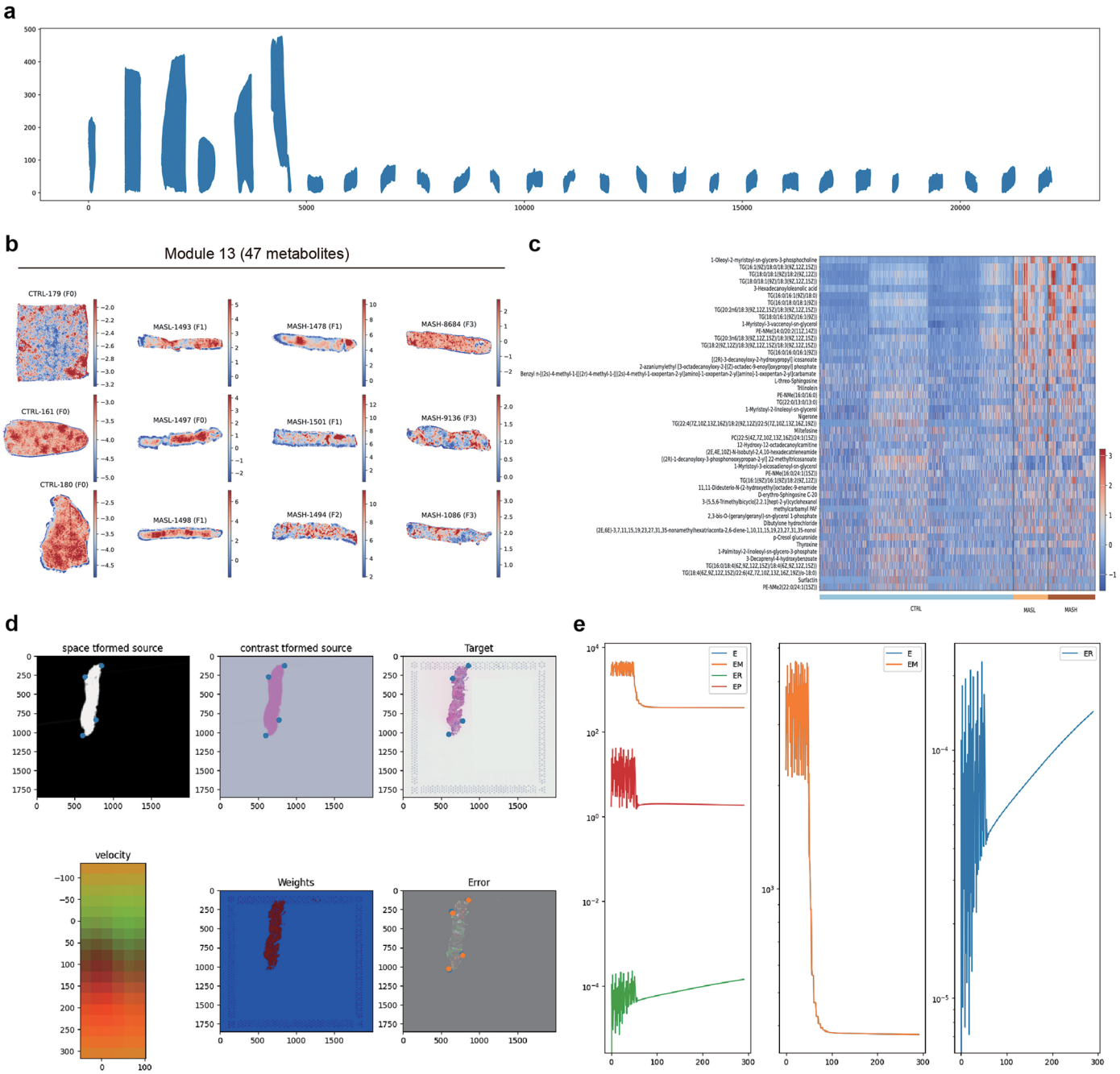

Extended Data Fig. 6 | Identification of spatial metabolic modules by Hotspot and alignment with ST via STalign. a, Rearrangement of the spatial coordinates $n = 27$ MALDI-MSI SM samples in the two-dimensional coordinate system. **b**, Spatial distribution of Hotspot-identified Module 13 across twelve representative tissue sections. **c**, 47 metabolites from Module 13 are presented as heatmap, with columns representing pixels within each disease status and rows displaying metabolite annotations. **d**, Overview of the alignment steps between MSI data points and H&E image of Visium ST by STalign. **e**, Key parameters that indicate the effects of spatial multimodal alignment.

nature portfolio

Corresponding author(s): Jin Chai, Fan Bai, Ming-Hua Zheng, Xinshou Ouyang

Last updated by author(s): Sep 22, 2025

Reporting Summary

Nature Portfolio wishes to improve the reproducibility of the work that we publish. This form provides structure for consistency and transparency in reporting. For further information on Nature Portfolio policies, see our Editorial Policies and the Editorial Policy Checklist.

Statistics

For all statistical analyses, confirm that the following items are present in the figure legend, table legend, main text, or Methods section.

n/a	Confirmed
☐	☒ The exact sample size (*n*) for each experimental group/condition, given as a discrete number and unit of measurement
☐	☒ A statement on whether measurements were taken from distinct samples or whether the same sample was measured repeatedly
☐	☒ The statistical test(s) used AND whether they are one- or two-sided *Only common tests should be described solely by name; describe more complex techniques in the Methods section.*
☒	☐ A description of all covariates tested
☐	☒ A description of any assumptions or corrections, such as tests of normality and adjustment for multiple comparisons
☐	☒ A full description of the statistical parameters including central tendency (e.g. means) or other basic estimates (e.g. regression coefficient) AND variation (e.g. standard deviation) or associated estimates of uncertainty (e.g. confidence intervals)
☐	☒ For null hypothesis testing, the test statistic (e.g. *F*, *t*, *r*) with confidence intervals, effect sizes, degrees of freedom and *P* value noted *Give P values as exact values whenever suitable.*
☒	☐ For Bayesian analysis, information on the choice of priors and Markov chain Monte Carlo settings
☒	☐ For hierarchical and complex designs, identification of the appropriate level for tests and full reporting of outcomes
☐	☒ Estimates of effect sizes (e.g. Cohen's *d*, Pearson's *r*), indicating how they were calculated

Our web collection on statistics for biologists contains articles on many of the points above.

Software and code

Policy information about availability of computer code

Data collection	No specific software was used for data collection. The datasets were processed and analyzed using the open source software listed below.
Data analysis	Celescope (v.1.15.0) was used to align and quantify scRNA-seq data to obtain a matrix for analysis. Space Ranger (v.3.1.1) was used to process spatial transcriptomics data to obtain a matrix for analysis. milo (v.2.0.0) was used to test for the differential abundance of cellls within defined neighborhoods. Scirpy (v.0.19.1) was used for scVDJ data analysis. Scanpy (v.1.10.3) was used for the downstream analysis after object creation and clustering the scRNA-seq datasets. flowsig (v.0.1.2) was used to identify differentially flowing signal variables. CellPhoneDB (v.5.0.0) and CellChat (v.2.1.2) was used to identify cell-cell interactions. CCplotR (v.0.99.3) was used to visualize significant ligand-receptor pairs. commot (v.0.0.3) was used to assess ligand-receptor interaction intensities within Visium sections. STAligner (v.1.0.0) was used for batch effect correction in Visium ST datasets. Cell2location (v.0.1.3) was used for the spots' deconvolution of Visium ST datasets. pyscenic (v.0.12.1) was used to infer gene regulatory networks from scRNA-seq datsets. igraph (v.2.0.3) and ggraph (v.2.1.0) were used for the visualization of gene regulatory networks. decoupler (v.1.6.0) was used for the enrichment of GO and KEGG terms. sctm (v.0.1.3) was used for the identification of spatial gene topics. Hotspot (v.1.1.1) was used to identify and display metabolic programs. STalign (v.1.0) was used to integrate spatial transcriptomics with spatial metabolomics. GraphPad Prism software (v.10.4.2) was used for experimental data statistical analysis and visualization.

The code required to reproduce the analyses in this paper is available through GitHub (github.com/OMIC-coding/Spatial_multiomics_analysis_MASLD) and Zenodo (doi.org/10.5281/zenodo.17192831).

For manuscripts utilizing custom algorithms or software that are central to the research but not yet described in published literature, software must be made available to editors and reviewers. We strongly encourage code deposition in a community repository (e.g. GitHub). See the Nature Portfolio guidelines for submitting code & software for further information.

Data

Policy information about availability of data

All manuscripts must include a data availability statement. This statement should provide the following information, where applicable:

- Accession codes, unique identifiers, or web links for publicly available datasets
- A description of any restrictions on data availability
- For clinical datasets or third party data, please ensure that the statement adheres to our policy

All raw data for scRNA-seq and 10x Visium generated in this study are deposited in the Genome Sequence Archive in National Genomics Data Center, China National Center for Bioinformation / Beijing Institute of Genomics, Chinese Academy of Sciences (GSA-Human: HRA007511) that are available under controlled access at https://ngdc.cncb.ac.cn/gsa-human; The spatial metabolomic data have been deposited in the OMIX, China National Center for Bioinformation / Beijing Institute of Genomics, Chinese Academy of Sciences (https://ngdc.cncb.ac.cn/omix: accession no.OMIX009098). The processed data of scRNA-seq and Visium ST are available from the OMIX with the accession number OMIX010136. The spatial proteomic data is also available from the OMIX under accession number OMIX009117. All processed data can be visualized and downloaded on the HMSMA website (https://db.genomics.cn/stomics/hmsma). Source data are provided with this paper.

Research involving human participants, their data, or biological material

Policy information about studies with human participants or human data. See also policy information about sex, gender (identity/presentation), and sexual orientation and race, ethnicity and racism.

Reporting on sex and gender	Information on sex is summarized in Supplementary Table 1. Sex and gender were not considered in the study design.
Reporting on race, ethnicity, or other socially relevant groupings	All 61 participants are Asian. Race, ethnicity, or other socially relevant groupings were not considered in study design.
Population characteristics	Control liver samples were procured from ten patients at the Institute of Hepatobiliary Surgery of Southwest Hospital, none of whom showed evidence of fatty liver disease, primary biliary cholangitis (PBC), autoimmune hepatitis (AIH), liver cancer, viral hepatitis, or other metabolic liver diseases. Samples from patients with MASLD were obtained through biopsy or surgical procedures. The diagnosis of MASLD was based on integrating clinical features, laboratory tests, and pathological diagnosis while excluding other known hepatic conditions.
Recruitment	The participants were diagnosed at the First Affiliated Hospital of Third Military Medical University and the First Affiliated Hospital of Wenzhou Medical University, fulfilling our pre-established inclusion criteria, voluntarily participating in the study. Prior to the commencement of the study, written informed consent was obtained from all participants.
Ethics oversight	The study protocol was reviewed and approved by the Ethics Committees of the First Affiliated Hospital (Southwest Hospital) of Army Medical University [approval nos. (A)KY2021061 and (B)KY202350] and the First Affiliated Hospital of Wenzhou Medical University [approval no. 2016-246].

Note that full information on the approval of the study protocol must also be provided in the manuscript.

Field-specific reporting

Please select the one below that is the best fit for your research. If you are not sure, read the appropriate sections before making your selection.

☒ Life sciences ☐ Behavioural & social sciences ☐ Ecological, evolutionary & environmental sciences

For a reference copy of the document with all sections, see nature.com/documents/nr-reporting-summary-flat.pdf

Life sciences study design

All studies must disclose on these points even when the disclosure is negative.

Sample size	A total of 29 liver samples were subjected to single-cell sequencing, including 6 controls, 7 MASL samples, 16 MASH samples. Liver tissue samples for spatial transcriptomics were collected from 35 donors, including 7 controls, 10 MASL samples, 18 MASH samples. Liver tissue samples for spatial metabolomics were collected from 27 donors, including 6 controls, 9 MASL samples, and 12 MASH samples. A total of 14 liver samples were subjected to spatial proteomic profiling, including 4 controls, 3 MASL samples, 7 MASH samples. No statistical method was used to predetermine sample size.
Data exclusions	No data were excluded from the analyses.
Replication	All in vitro experiments were repeated independently at least three times.

Randomization	No randomization was used in the study because the patient data is observational.
Blinding	The investigators were not blinded to allocation during experiments and outcome assessment.

Reporting for specific materials, systems and methods

We require information from authors about some types of materials, experimental systems and methods used in many studies. Here, indicate whether each material, system or method listed is relevant to your study. If you are not sure if a list item applies to your research, read the appropriate section before selecting a response.

Materials & experimental systems

n/a	Involved in the study
☐	☒ Antibodies
☐	☒ Eukaryotic cell lines
☒	☐ Palaeontology and archaeology
☒	☐ Animals and other organisms
☒	☐ Clinical data
☒	☐ Dual use research of concern
☒	☐ Plants

Methods

n/a	Involved in the study
☒	☐ ChIP-seq
☒	☐ Flow cytometry
☒	☐ MRI-based neuroimaging

Antibodies

Antibodies used	All antibodies used in the study are listed in the Supplementary Table 3. TREM2, Cell Signaling, Danvers, MA/91068 MITF, Abcam, Cambridge, MA/ab303530 CYP3A4, Santa Cruz, Santa Cruz, CA/sc-53850 EPCAM, Cell Signaling, Danvers, MA/14452 HNF4a, Cell signaling, Danvers, MA/3113 Ki67, Abcam, Cambridge, MA/ab16667 MET, Cell signaling, Danvers, MA/8198S Mouse IgG, Absin, Shanghai, China/abs50012 Rabbit IgG, Absin, Shanghai, China/abs50012
Validation	All antibodies used in the study are commercially available with validation procedures described on the sites of the manufacture. TREM2, https://www.cellsignal.cn/products/primary-antibodies/trem2-d8i4c-rabbit-mab/91068 MITF, https://www.abcam.cn/products/primary-antibodies/mitf-antibody-epr26363-10-ab303530.html CYP3A4, http://www.scbt.com/p/cyp3a4-antibody-hl3 EPCAM, http://www.cellsignal.cn/products/primary-antibodies/epcam-d9s3p-rabbit-mab/14452 HNF4a, http://www.cellsignal.cn/products/primary-antibodies/hnf4a-c11f12-rabbit-mab/3113 MET, http://www.cellsignal.cn/products/primary-antibodies/met-d1c2-xp-rabbit-mab/8198 Ki67, http://www.abcam.cn/products/primary-antibodies/ki67-antibody-sp6-ab16667.html Mouse IgG, https://www.absin.cn/four-color-multi-label-immunofluorescence-kit/abs50012.html Rabbit IgG, https://www.absin.cn/four-color-multi-label-immunofluorescence-kit/abs50012.html

Eukaryotic cell lines

Policy information about cell lines and Sex and Gender in Research

Cell line source(s)	THP-1 and HepG2 cell lines were purchased from Hunan Fenghui Biotechnology Co., Ltd, China.
Authentication	Cell line authentication was performed for THP-1 and HepG2 via Short Tandem Repeat (SRT) profiling prior to experimentation. Each profile matched the known reference standard.
Mycoplasma contamination	All cell lines were tested for Mycoplasma by PCR, and the results were negative for Mycoplasma contamination.
Commonly misidentified lines (See ICLAC register)	No commonly misidentified cell lines were used in this study.

Plants

Seed stocks	*Report on the source of all seed stocks or other plant material used. If applicable, state the seed stock centre and catalogue number. If plant specimens were collected from the field, describe the collection location, date and sampling procedures.*
Novel plant genotypes	*Describe the methods by which all novel plant genotypes were produced. This includes those generated by transgenic approaches, gene editing, chemical/radiation-based mutagenesis and hybridization. For transgenic lines, describe the transformation method, the number of independent lines analyzed and the generation upon which experiments were performed. For gene-edited lines, describe the editor used, the endogenous sequence targeted for editing, the targeting guide RNA sequence (if applicable) and how the editor was applied.*
Authentication	*Describe any authentication procedures for each seed stock used or novel genotype generated. Describe any experiments used to assess the effect of a mutation and, where applicable, how potential secondary effects (e.g. second site T-DNA insertions, mosiacism, off-target gene editing) were examined.*